Scientific report of the project COMpton Polarimeter with Avalanche Silicon readout (COMPASS)

Bando TECNO INAF 2014

Ettore Del Monte (IAPS, Responsabile Scientifico Nazionale)

Research Unit 1 (IAPS): Armando Brandonisio, Enrico Costa, Sergio Di Cosimo, Giuseppe Di Persio, Sergio Fabiani, Enrico Massaro, Alfredo Morbidini, Ennio Morelli, Fabio Muleri, Luigi Pacciani, Alda Rubini, Paolo Soffitta (IAPS)

Research Unit 2 (IASF-Palermo): Salvatore Giarrusso, Teresa Mineo, Giuseppe Sottile, Domenico Impiombato (IASF Palermo), Sergio Guido Michele Billotta (Osservatorio di Catania)

19/1/2018

Responsabile Scientifico Nazionale

Dr. Ettore Del Monte

Ettore Del Monte

Direttore dell'IAPS

Dr. Fabrizio Capaccioni

Fabrizio Capaccioni

Direttore dell'IASF-Palermo

Dr. Giancarlo Cusumano

Giancarlo Cusumano

1 Objective of the project

The measurement of the polarisation of X-rays expands the observation space by simultaneously adding two observable quantities, the degree and the angle of polarisation, to the set of source properties currently measured (energy, time, and localisation) [1]. Polarimetry will thus open new dimensions for understanding how X-ray emission is produced in astrophysical objects, especially for systems under extreme physical conditions, such as neutron stars and black holes [1]. In fact, polarisation by itself probes physical anisotropies, such as those produced by ordered magnetic fields, aspheric matter distributions, or general relativistic coupling to black-hole spin, that are not otherwise measurable [1].

A polarimeter based on the imaging of tracks produced after the photoelectric absorption of X-rays in a gas cell and sensitive in the energy band between ~2 keV and ~10 keV has been developed by Costa et al. (2001) and is described in Ref. [2]. This polarimeter is now in the focal plane instrumentation of the IXPE mission, approved by NASA at the beginning of 2017 [3] and due for launch in mid-2021. At higher energy, where the cross section of the photoelectric effect is too low to be practically useful, we can exploit the Compton effect to measure the polarisation of X-rays.

In particular, from the differential cross-section of the Compton effect, we can see that the modulation factor $\mu(\theta)$, i.e. the response of the instrument to fully linearly polarised radiation, is defined as

$$\mu(\theta) = \frac{N_{max}(\theta) - N_{min}(\theta)}{N_{max}(\theta) + N_{min}(\theta)} = \frac{(d\sigma/d\Omega)_{\phi=\pi/2} - (d\sigma/d\Omega)_{\phi=0}}{(d\sigma/d\Omega)_{\phi=\pi/2} + (d\sigma/d\Omega)_{\phi=0}} = \frac{\sin^2\theta}{E_0/E_1 + E_1/E_0 - \sin^2\theta}$$

Where θ is the scattering angle in Compton effect, E_0 is the energy of the incident photon, E_1 is the energy of the scattered photon,

$$\frac{E_1}{E_0} = \frac{1}{1 + E_0/m_e c^2(1 - \cos\theta)}$$

Therefore, the ideal polarimeter would use photons scattered at 90° angle, and work in the Thomson limit. Furthermore, it should select as much as possible photons scattered only once, because the directions of the photons are randomised after a few scatterings, and the memory of the initial polarisation is therefore lost [4]. A plot of the modulation factor as a function of the scattering angle θ for different energies between 22 keV and 511 keV from Ref. [5] is shown in Figure 1. It is evident from Figure 1 that the modulation factor is higher for lower energy photons and that the maximum occurs at a scattering angle near 90°.

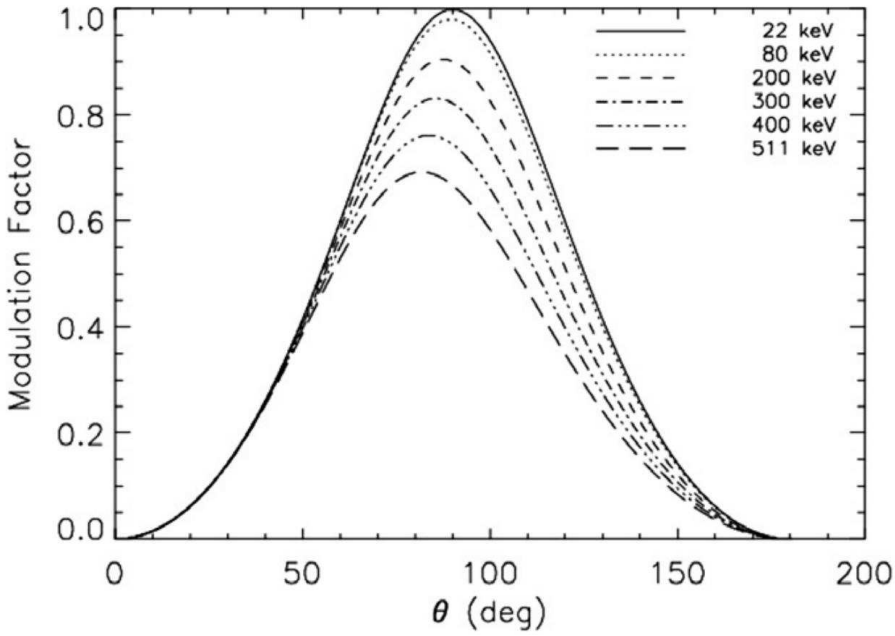

Figure 1: Modulation factor as a function of the scattering angle θ at different energies from [5]. Linearly polarized low energy radiation gives a higher modulation factor and the maxima occur for scattering angles approaching 90°.

Costa et al. (1995) in Ref. [4] classify Compton scattering polarimeters as

- "one-phase" if the detector is built using the same material for both the scattering and the absorption stages;
- "two-phases" if the polarimeter employs two different materials for the two stages.

One-phase low-Z polarimeters, given that in most cases only a fraction of the initial energy is detected, provide a poor reconstruction of the photon energy and, since the modulation strongly depends on the energy, any result would be very ambiguous. On the contrary, a high-Z material for both the scatterer and the absorber gives a good spectral response but the competition of absorption and scattering in the two stages results in a much higher threshold. In practice such a device is effective only at the energies where we have the transition from the prevailing photoelectric to the prevailing Compton. Two-phases instruments, composed of a low-Z scatterer and a high-Z absorber are the best combination: the low-Z material guarantees a high scattering probability even at energies as low as ~20 keV and the high-Z material detects the largest fraction of the photon energy and provides a good energy reconstruction and spectral resolution.

If we use an "active" scatterer, i.e. a detector which produces a signal when a photon is scattered, we can significantly reduce the background by operating the scattering and absorbing stages in coincidence. Good candidates for both stages are scintillator detectors, which are produced with both low-Z and high-Z materials. Since the residual background by chance occurrence within time window of the polarimeter depends on the width of this window in the coincidence between scattering and absorbing stages, this polarimeter requires to use for the scintillators a read-out system whose signal is shorter than ~1 μs. The background contains an additional component, represented by double events, produced e.g. by the ionisation of charged particles, which do not depend on the width of the coincidence window. To remove these events, techniques of spatial coincidence and image analysis can be used, similar to the ones used e.g. in Cherenkov Imaging Telescopes. In addition, a finely sub-divided detector, obtained with scintillators of few mm^2 cross-

section and few cm length, allows to better reconstruct the scattering position and angle with a substantial improvement of the sensitivity and a reduction of the systematics.

For this purpose we select Silicon Photomultipliers (SiPM) as the read-out elements for the scintillators. SiPM are innovative photodetectors that have now reached a high level of readiness as fast readout devices for scintillators. In addition, SiPMs are compact, robust, insensitive to magnetic fields and are typically supplied at 50 – 70 V, compared to a high voltage of the order of ~kV for the photomultiplier tubes (PMTs). For this reasons, SiPMs are particularly suitable for space application. Moreover SiPMs have a small mass, potentially smaller than that of a small sensing element. It can be conceived to have a detector finely subdivided in 3D space, which is not feasible with glass PMs with their HV Power Supplies and potted dividers.

The scientific objective of COMPASS is the demonstration of the feasibility of a Compton-effect polarimeter using SiPMs as readout elements. In addition we plan to study as front-end electronic element the CITIROC ASIC, already used with SiPMs for Cherenkov Imaging Telescopes [6].

2 Personnel involved in the project

2.1 IAPS Research Unit

Unità di Ricerca 1: IAPS					
Nome	**Affiliazione**	**Posizione**	**Ruolo**	**Primo anno (mesi)**	**Secondo anno (mesi)**
Ettore Del Monte	IAPS	Tecnologo	Coordinamento, misure di laboratorio e analisi dati, esperienza sui GRBs	4	4
Luigi Pacciani	IAPS	Ricercatore	Misure di laboratorio e analisi dati	2	2
Paolo Soffitta	IAPS	Primo ricercatore	Esperienza di Polarimetria	1	1
Enrico Costa	IAPS	Associato	Esperienza di Polarimetria	2	2
Ennio Morelli	IASF-Bologna	Associato	Esperienza sui sistemi di acquisizione	1	1
Enrico Massaro	IAPS	Associato	Algoritmi, requisiti scientifici	2	2

Fabio Muleri[1]	IAPS	Assegno di Ricerca su questo progetto	Esperienza di Polarimetria	6	0
Armando Brandonisio[2]	IAPS	Laureando	Test di SiPM in laboratorio e analisi dati	6	4
Sergio Fabiani[3]	IAPS	Assegno di Ricerca cofinanziato da questo progetto	Test di ASIC in laboratorio e analisi dati	0	6
Alda Rubini	IAPS	CTER	Sistemi di readout e acquisizione, Misure di laboratorio e analisi dati	3	3
Giuseppe Di Persio	IAPS	CTER	System administration, web	1	1
Alfredo Morbidini	IAPS	CTER	Produzione di parti di meccanica	1	1
Sergio Di Cosimo	IAPS	OT	Program management e rendicontazione	2	2
Totale				**31**	**29**

[1]Fabio Muleri left the COMPASS project after six months of Assegno di Ricerca and had a Contratto a Tempo Determinato as Researcher on the XIPE Project;

[2]Armando Brandonisio was involved in COMPASS for his Laurea thesis at the University of Rome "La Sapienza" but he did not finish the thesis and did not graduate;

[3]Sergio Fabiani had an Assegno di Ricerca co-funded by the COMPASS and XIPE projects with equal time shares (six months on COMPASS and six on XIPE).

2.2 IASF-Palermo Research Unit

Unità di Ricerca 2: IASF-Palermo					
Nome	**Affiliazione**	**Posizione**	**Ruolo**	**Primo anno (mesi)**	**Secondo anno (mesi)**
Salvatore Giarrusso	IASF Palermo	Ricercatore	Esperienza sui SiPMs per IACT	1.4	1.4
Teresa Mineo	IASF Palermo	Ricercatore	Simulazione delle performance di SiPM, requisiti scientifici	1.4	1.4

Giuseppe Sottile	IASF Palermo	Tecnologo	Misure di laboratorio e analisi dati	1.4	1.4
Sergio Guido Michele Billotta	Osservatorio di Catania	Tecnologo	Esperienza sui SiPM, caratterizzazione e calibrazione dei SiPM	1.4	1.4
Domenico Impiombato	IASF Palermo	Contratto già attivato	Misure di laboratorio e analisi dati	2.0	0.0
Totale				**7.6**	**5.6**

Mesi totali dedicati al progetto					
			Ruolo	**Primo anno (mesi)**	**Secondo anno (mesi)**
			Ricercatori e tecnologi strutturati	12.6	12.6
			Associati all'INAF	5.0	5.0
			Post-doc (borsisti e assegnisti)	6.0	6.0
			Laureandi	6.0	4.0
			Tecnici	7.0	7.0
Totale				**36.6**	**34.6**

3 Budget Report

3.1 Research Unit 1 (IAPS)

In the approved budget we requested for the Research Unit 1 (IAPS) 1.5 years of Assegno di Ricerca, corresponding to 51000 EUR. As specified in sec. 2.1 above, Fabio Muleri left the COMPASS project after six months and another Assegno di Ricerca could be issued only for six months, co-funded between COMPASS and XIPE. Consequently, only 1 year of Assegno di ricerca was spent instead of 1.5 years funded. The remaining funds were distributed to the other budget components.

3.2 Research Unit 2 (IASF-Palermo)

With respect to the approved budget, we moved most of the funds to the Instrumentation component in order to purchase a laser illumination system to characterise silicon sensors (SiPMs) and the associated front-end electronic, and to the Consumables to purchase the CITIROC evaluation

boards. This purchase is necessary to calibrate with very narrow light pulses (<1 ns), not available with the LED already in the laboratory of IASF-Palermo.

4 Conferences and publications

During the time frame of the TECNO-INAF 2014 grant

we published the paper:

- E. Massaro, S. Fabiani, R. Campana, E. Costa, E. Del Monte, F. Muleri, P. Soffitta, "*Correlation methods for the analysis of X-ray polarimetric signals*", **Nuclear Instr. and Methods in Phys. Res. A, 885, 7 – 14 (2017)**

and we presented two posters at the conference "SPIE Astronomical Telescopes + Instrumentation 2016" (26 June – 1 July 2016 Edinburgh, Scotland, UK). Both posters are published in the conference proceedings:

- E. Del Monte, A. Rubini, A. Brandonisio, F. Muleri, P. Soffitta, E. Costa, G. Di Persio, S. Di Cosimo, E. Massaro, A. Morbidini, E. Morelli, L. Pacciani, S. Fabiani, D. Michilli, S. Giarrusso, O. Catalano, D. Impiombato, T. Mineo, G. Sottile, S. Billotta, "*Silicon photomultipliers as readout elements for a Compton effect polarimeter: the COMPASS project*", **Procs. SPIE 9915, id. 991528 13 pp. (2016)**
- E. Massaro, E. Del Monte, F. Massa, R. Campana, F. Muleri, P. Soffitta, E. Costa, "*Geometrical tools for the analysis of x-ray polarimetric signals*", **Procs. SPIE 9905, id. 99054I 6 pp. (2016)**

5 Main results of the COMPASS project

5.1 The Compton effect polarimeter

Following the definition given in Sec. 1 (from Ref. [4]), in COMPASS we study a two phases polarimeter. The scattering stage is based on low-Z scintillator and is in charge of producing a signal when the photon is scattered; the absorption stage contains a high-Z scintillator which stops the scattered photon and measures the energy. To reduce the background, the two stages operate in coincidence with a time window of the order of ~1 μs. In COMPASS both scattering and absorption stages are obtained with a small rod of scintillator. To reach the signal duration short enough to employ a coincidence window of the order of ~1 μs, we study the SiPM as the read-out sensor for scintillators.

We recall here that the scattering elements are required to have low-Z to have a favorable ratio between the probability of Compton scattering and photoelectric absorption, and a short pulse duration to use a short coincidence time window. For this reason we tested three different types of plastic scintillators, produced by the Eljen company and showing these characteristics: EJ-204, EJ-200 and EJ-260. The three materials have a similar light yield of ~10 photons / keV and a pulse duration of few ns. We procured from Eljen Technologies these scintillators as rods with a square section of 3 mm × 3 mm (same as the SiPM sensitive area) and length of 3, 6 and 10 cm.

List of the plastic scintillators purchased from Eljen Technologies:

- EJ-200
    - two samples of 3 mm × 3 mm area and 6 cm length;
- EJ-204
    - two samples of 3 mm × 3 mm area and 3 cm length;
    - two samples of 3 mm × 3 mm area and 6 cm length;
    - two samples of 3 mm × 3 mm area and 10 cm length;
- EJ-260
    - two samples of 3 mm × 3 mm area and 6 cm length.

The spectrum of the scintillation photons well matches the interval of wavelength with highest photon detection efficiency in the selected SiPMs (380 – 550 nm). The three different materials are characterised by different spectrum of the light emission, resulting in a different efficiency when the quantum efficiency of the SiPM is considered.

We tested two different materials as wrapping for the scintillator rods: Polytetrafluoroethylene (PTFE) tape and VM2000 reflective paper.

In the COMPASS scheme, the absorber is in charge of measuring the energy of the scattered photon and simultaneously provide a trigger signal for the coincidence system. Since in the Compton effect only a small fraction of the photon energy is deposited in the scattering stage, the absorber detects most of the incident energy. Assuming a Compton scattering angle of 90°, the ratio between the energy of the scattered and incident photon is 96 % at 20 keV, 91 % at 50 keV and 84 % at 100 keV. For this reason we require for the absorber a high quantum efficiency up to high energy, a good linearity over the whole energy range and a good energy resolution. A specific problem of Scintillators id hygroscopicity. The main conventional material, Tallium activated NaI, is highly hygroscopic. It must be canned within a leak tight box with an optical window, typically of glass or quartz. This implies an extra-mass, an addition of optical interfaces, with the related loss, and increased mechanical constraints. Moving from a set of large detectors to a finely subdivided detecting assembly the ratio surface/volume diverges and a detector requiring a leak tight canning is progressively less competitive. Therefore in the present study we consider mandatory that the detectors are not hygroscopic.

The requirements of the absorption stage are:

- non hygroscopic;
- light emission wavelength compatible with the peak quantum efficiency of SiPMs (380 – 550 nm);
- pulse duration < ~1 μs to "fit" in a narrow coincidence window with the scattering stage;
- high photoelectric quantum efficiency between ~20 keV and ~150 keV;
- high light yield and good spectral resolution;
- vacuum resistant (for space applications).

We chose for the absorption stage a commercially available material which fulfills our requirements, $Gd_3Al_2Ga_3O_{12}$ activated with Ce (hereafter GAGG), produced by Furukawa company. The GAGG rods have a square section of 3 mm × 3 mm and a length of 3 cm, and are wrapped with PTFE tape. In particular, the GAGG performances compared with the requirements listed above, are:

- non hygroscopic;
- the peak of the light emission is at 520 nm [7]
- the decay times are (127 ± 6) ns with 85 % intensity and (530 ± 30) ns with 15 % intensity [8]
- the density is 6.63 g / cm^3 [7] and the total absorption efficiency (photoelectric and Compton effects) for 3 mm thickness is ~100 % up to ~100 keV and ~50 % at 200 keV;
- the light yield is 57 photons / keV [7] , the energy resolution measured with a PMT is 6.1 % at 662 kev (^{137}Cs) [8]
- vacuum resistant (for space applications).

SiPM are solid-state detectors composed of an array of microcells operated at Geiger-mode and able to reach a gain of ~10^6 with a bias voltage ranging between 50 V and 70 V. As shown in Figure 2, SiPMs are small and compact and, for this reason, are particularly suitable for space applications.

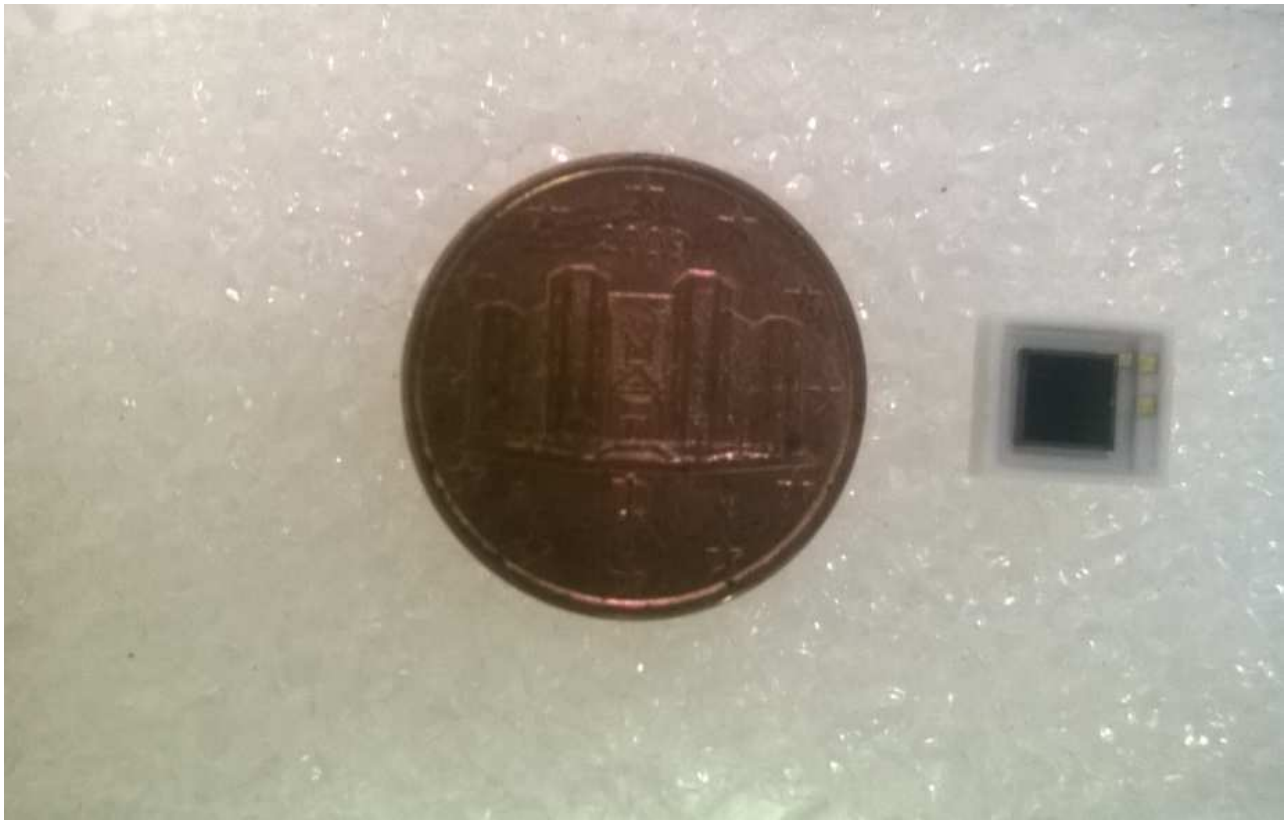

Figure 2: Picture of the SiPM by Hamamatsu, compared to a 1 cent EUR coin

SiPMs are a key technology for COMPASS because they produce short pulses of the order of tens of ns with amplitude linearly proportional to the number of photons detected from the scintillator following the absorption of one gamma-ray photon. For this reason SiPMs allow to measure the amplitude, proportional to the energy, of the detected photon, especially in the absorption stage. SiPMs are developed for a large number of applications (especially in the field of medical instrumentation) and are thus a rapidly evolving technology. The dark current rate, i.e. the counting rate produced even without detection of photons, is still two – three orders of magnitude higher in a SiPM than in a PMT. For this reason, most of the effort of the technological development of SiPMs is in the reduction of the dark current rate. For example, Hamamatsu is reducing the dark current rate by reducing the cross-talk between adjacent pixels.

5.2 Characterisation of SiPMs as read-out sensors for scintillators

5.2.1 Experimental set-up to measure the performances of a single SiPM with organic and inorganic scintillators

5.2.1.1 Instrumentation purchased to develop this experimental set-up:

- Four Hamamatsu C12332 driving circuits for SiPM with dedicated cables;
- Eight samples of SiPM S13360-3050CS from Hamamatsu;
- Three inorganic GAGG scintillator rods (3 mm × 3 mm × 3 cm) wrapped with PTFE tape;
- Ten rods of organic scintillator:
    - two samples of EJ-200 (3 mm × 3 mm × 6 cm),
    - two samples of EJ-204 (3 mm × 3 mm × 3 cm),
    - two samples of EJ-204 (3 mm × 3 mm × 6 cm),
    - two samples of EJ-204 (3 mm × 3 mm × 10 cm),
    - two samples of EJ-260 (3 mm × 3 mm × 6 cm).
- Custom structure to hold the SiPM and the scintillator rod during the test, designed by us and produced by the mechanical workshop at IAPS (see Figure 3 and Figure 6)

5.2.1.2 Description of the experimental set-up

We purchased from Hamamatsu eight samples of SiPMs S13360-3050CS, all of the fifth generation of low cross-talk sensors (LCT5) with a sensitive area of 3 mm × 3 mm and microcells pitch of 50 µm. the SiPMs are encapsulated in a ceramic package (see Figure 2).

In addition, we purchased from Hamamatsu four C12332 driving circuits, each one composed of two boards: the sensor board, with four sockets to accommodate different types of SiPMs, and the power supply board, providing the bias voltage with temperature feedback (see Figure 3). The sensor and power boards are connected with a flat cable of ~5 cm length. Only one SiPM at a time can be connected to the C12332 board.

The C12332 circuit is supplied with ±5 V and can be controlled by a PC via a USB cable. The circuit provides on an SMB output connector the analogue signal from the preamplifier (located in the power supply board). The preamplifier can be excluded and the load resistance can be selected between 50 Ω and 1 kΩ. We used C12332 circuits two different values of the preamplifier gain: 21 (default value) for the absorbing stage and 100 (enhanced value) for the scattering stage.

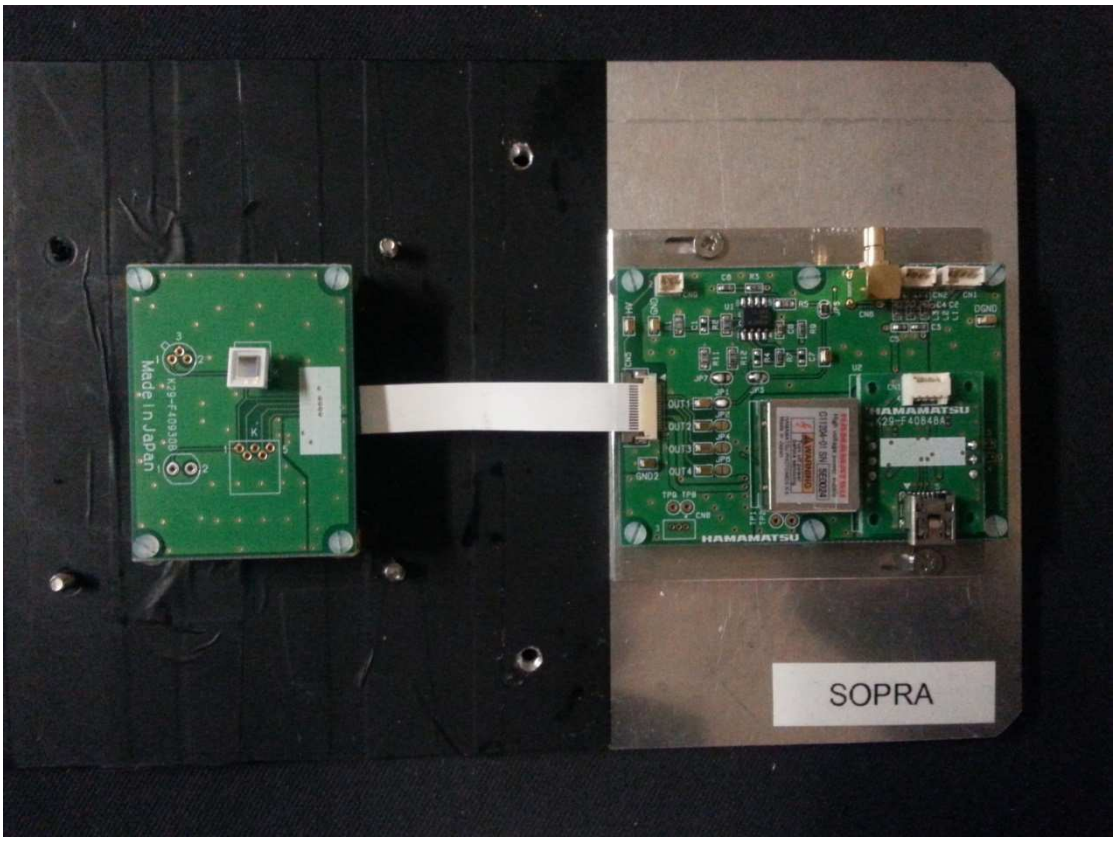

Figure 3: Picture of the C12332 driving circuit mounted on the support structure. The sensor board is on the left, the power supply board is on the right

An example of the output signal from the preamplifier on the C12332 driving circuit obtained with a SiPM and a light source of 0.01 µCi activity (composed of ^{241}Am diluted in plastic scintillator) is shown in Figure 4. The total duration of the signal is ~100 ns and the peaking time is shorter than 10 ns.

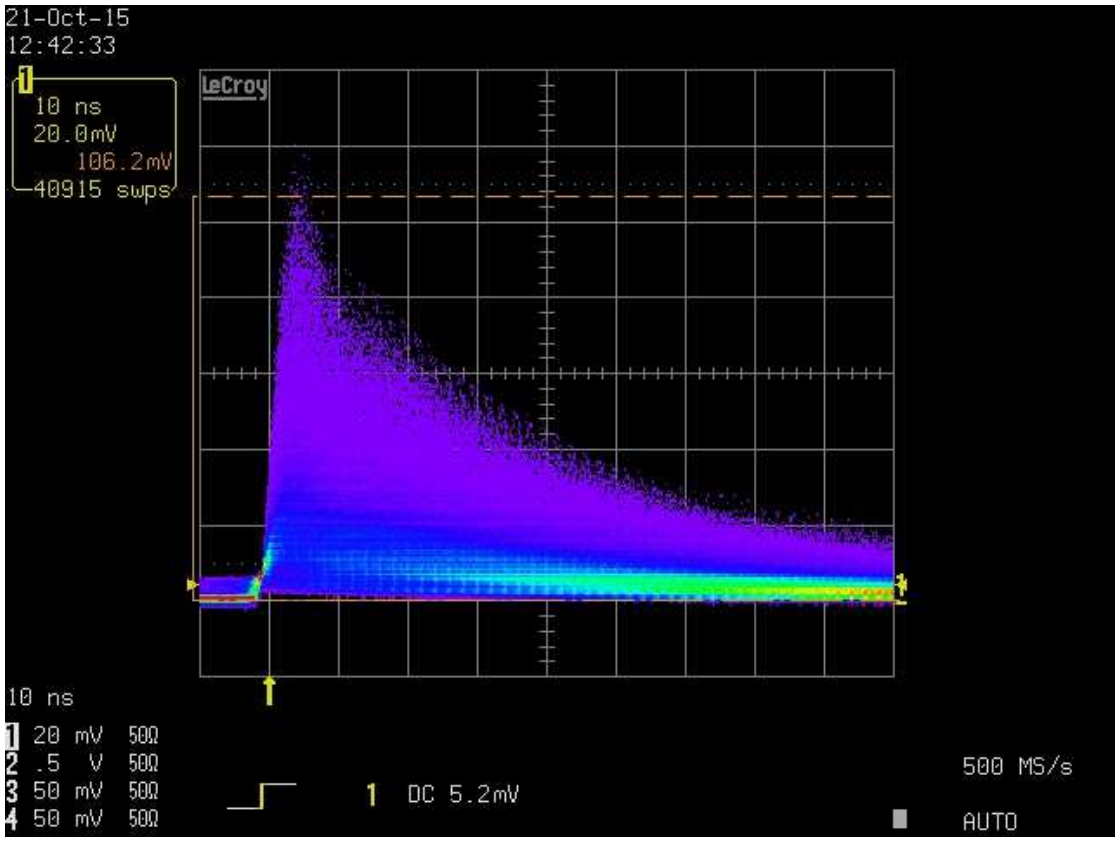

Figure 4: Output signal from the SiPM connected to the preamplifier of the C12332 driving circuit. The total duration of the signal is ~100 ns and the peaking time is shorter than 10 ns.

5.2.2 Characterisation with inorganic scintillators (GAGG)

5.2.2.1 Scientific goals

The scientific goals of this characterisation is the measurement of the linearity and energy resolution of the prototype of the absorbing stage, composed of a GAGG rod (3 mm × 3 mm × 3 cm) and a SiPM Hamamatsu 13360-3050CS with 50 µm pitch. The GAGG rod is wrapped with PTFE tape of the order of 250 – 300 µm thickness.

5.2.2.2 Experimental set-up

The scintillator rod is coupled to the SiPM entrance window using a drop of optical grease for scintillators. The SiPM is connected to the C12332 driving circuit, whose preamplifier has a gain value of 21. We process the analogue signals from the C12332 circuit using an electronic chain composed of the Research Amplifier Ortec 450 and a multichannel analyser Amptek MCA 8000A[1]. We show a block diagram of the experimental set-up in Figure 5. In the measurements we used the mechanical structure shown in Figure 6. The Sensor board with the SiPM and the scintillator rod is covered with a light tight box (not shown in the picture in Figure 3).

[1] http://www.amptek.com/pdf/mca8000a.pdf

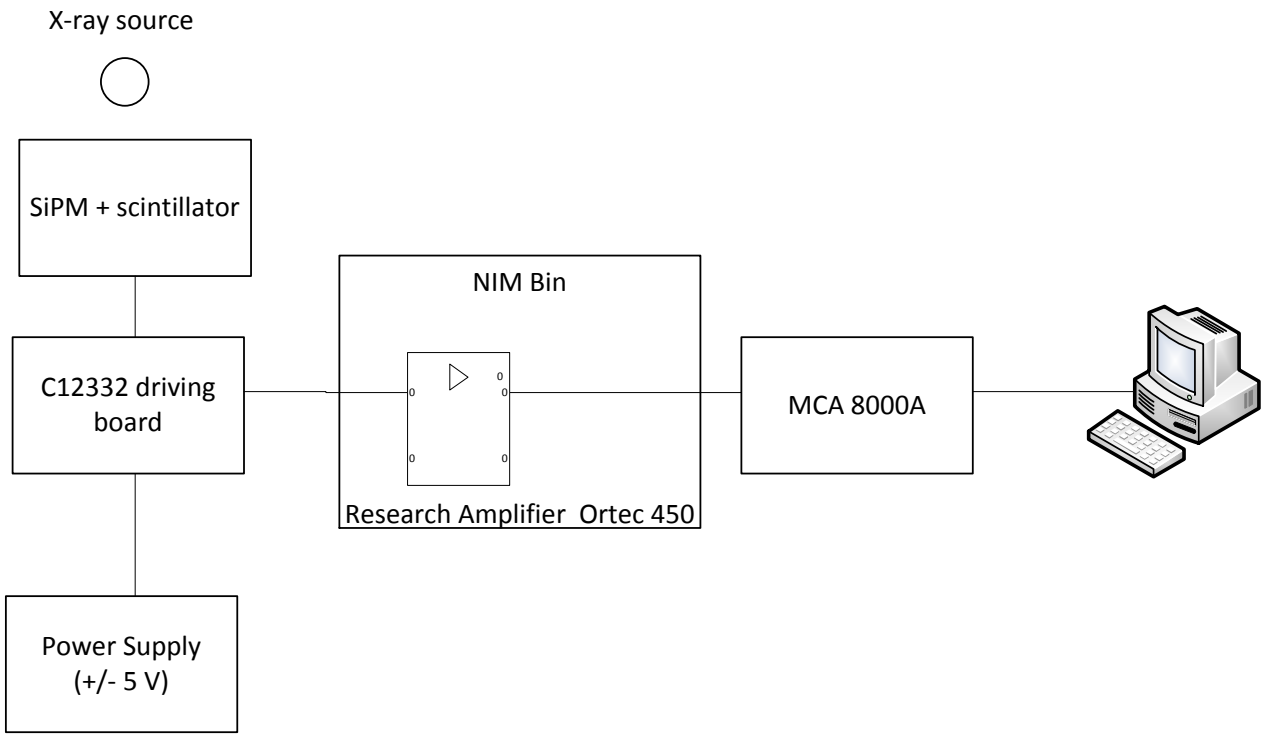

Figure 5: Block diagram of the experimental set-up

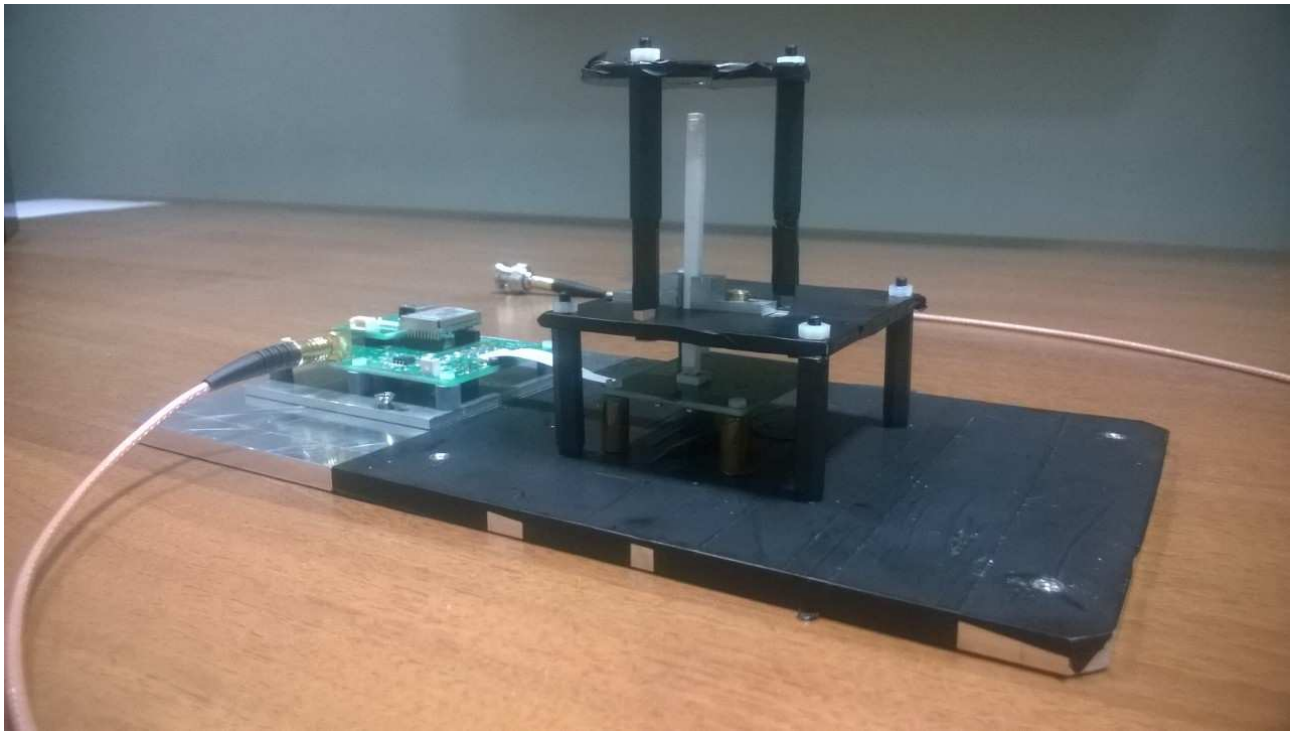

Figure 6: Picture of the experimental set-up. The power supply board is on the left, connected with the flat cable to the sensor board (center). The SiPM is placed on the sensor board. In the picture, the detector on top of the SiPM is a plastic scintillator rod. The light tight box to cover the sensor board and the mechanical structure is fixed to the four threaded holes. The black tape is used to reduce the reflection of stray light from the environment.

5.2.2.3 Results

5.2.2.3.1 Spectra of X-ray sources

We show for example the spectra of X-ray lines accumulated with the GAGG absorption stage: 5.9 keV (from ^{55}Fe, see Figure 7), 22.0 and 24.9 keV (from ^{109}Cd, see Figure 8), 59.5 keV (from ^{241}Am, see Figure 9), and 662 keV line from ^{137}Cs (shown in Figure 10). The dark current rate, partially overlapping with the 5.9 keV line, is empirically modeled with an exponential function (see Figure 7). From the system linearity (in Figure 11), the valley between the dark current rate and the X-ray line is at 3.3 ± 0.1 keV.

The energy resolution does not allow to resolve the two lines at 22.0 keV and 24.9 keV in the spectrum of ^{109}Cd, consequently we fit them with the sum of two Gaussian functions. The parameters of the gaussians are constrained as follows: the position from the energy of the X-ray lines and the area from the branching ratio. We assume the same σ for the two gaussians.

We empirically model the Compton edge on the left of the 662 keV line of the ^{137}Cs source as the product of a Gauss error function and an exponential function (see Figure 10) following the guidelines in Ref. [9].

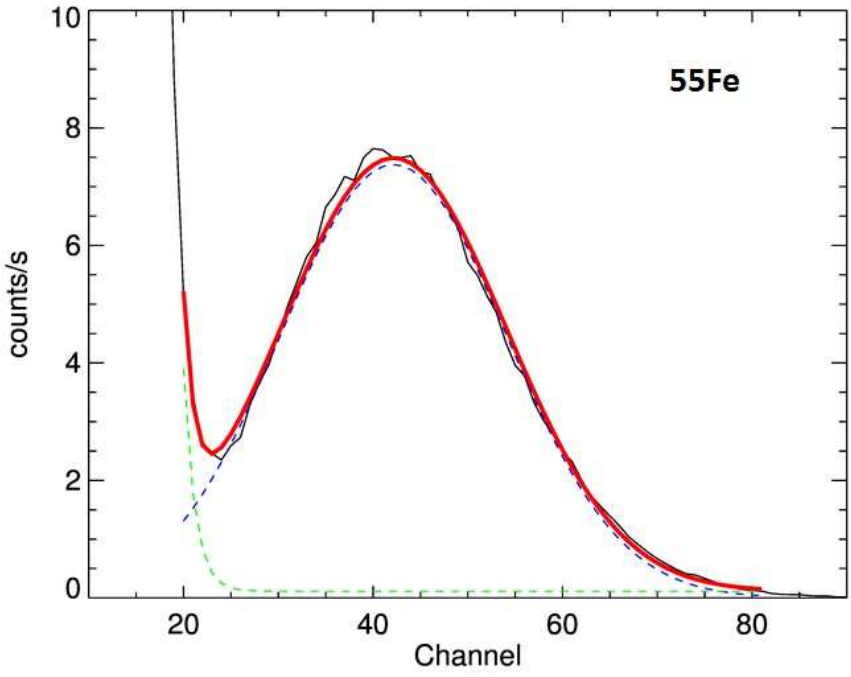

Figure 7: Spectrum of the 5.9 keV line of ^{55}Fe detected with the GAGG rod (3 mm × 3 mm × 30 mm) and the LCT5 SiPM at the nominal overvoltage value of +3 V. The blue dashed line is the gaussian fit of the X-ray line, the green dashed line is the exponential fit of the dark current rate. The x axis does not start from 0 Channels.

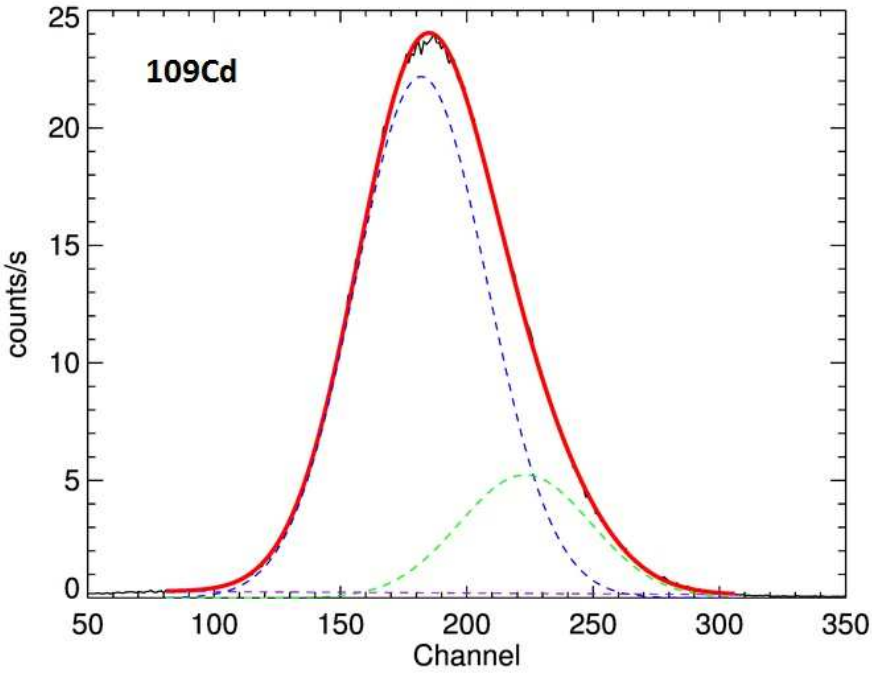

Figure 8: Spectrum of the 22.0 and 24.9 keV lines of ^{109}Cd detected with the GAGG rod (3 mm × 3 mm × 30 mm) and the LCT5 SiPM at the nominal overvoltage value of +3 V. The blue dashed line is the gaussian fit of the line at 22 keV, the green dashed line is the gaussian fit of the line at 24 keV, the purple dashed line is the background. The x axis does not start from 0 Channels.

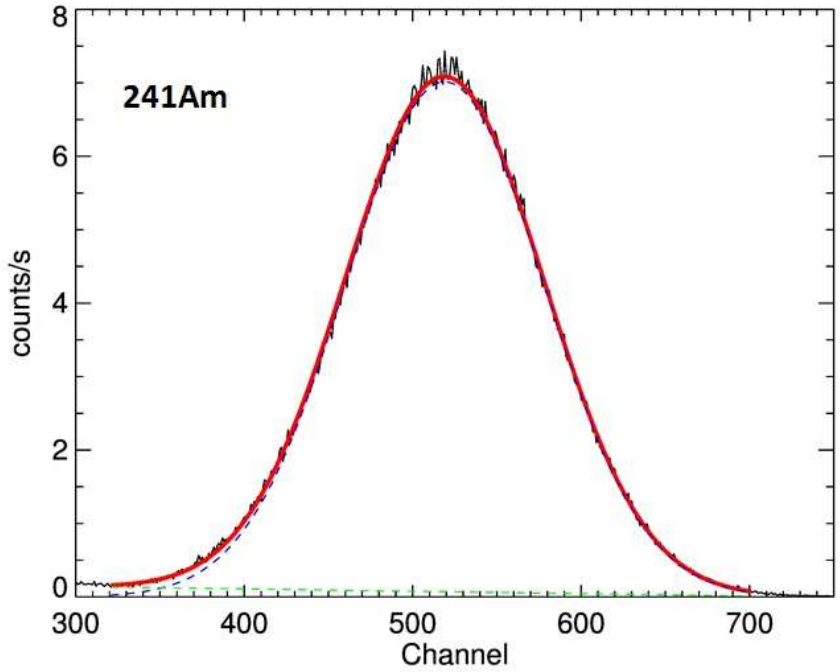

Figure 9: Spectrum of the 59.5 keV line of ^{241}Am detected with the GAGG rod (3 mm × 3 mm × 30 mm) and the LCT5 SiPM at the nominal overvoltage value of +3 V. The blue dashed line is the gaussian fit of the X-ray line, the green dashed line is the background. The x axis does not start from 0 Channels.

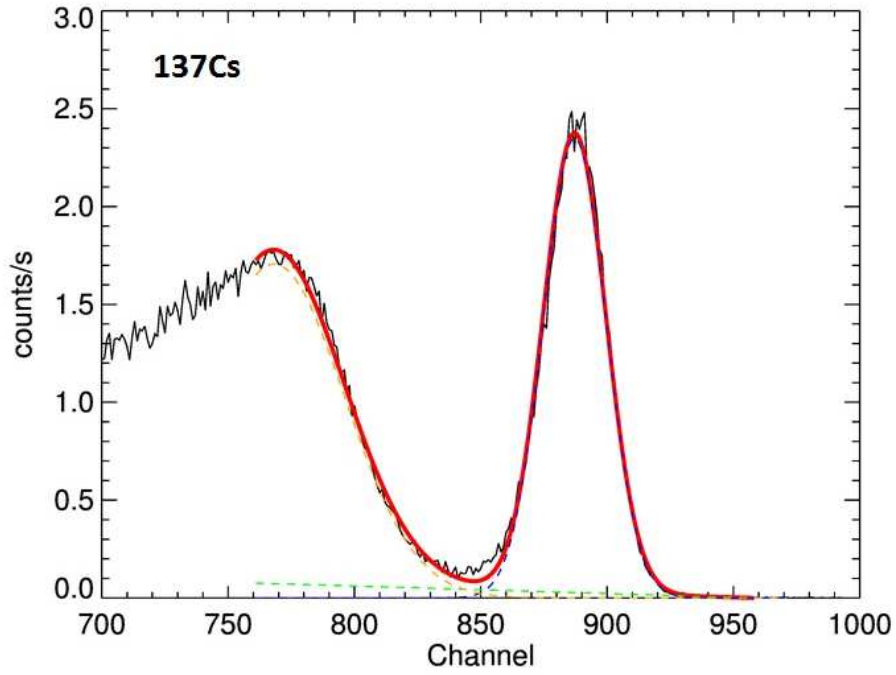

Figure 10: Spectrum of the 662 keV line of ^{137}Cs detected with the GAGG rod (3 mm × 3 mm × 30 mm) and the LCT4 SiPM (75 µm pitch) at the nominal overvoltage value of +3 V. The blue dashed line is the gaussian fit of the X-ray line, the green dashed line is the background and the orange dashed line is the empirical fit of the Compton edge (modelled as the product of a Gauss error function and an exponential function, following the guidelines by Cucoanes). The x axis does not start from 0 Channels.

5.2.2.3.2 Linearity of the system and energy resolution

By fitting the spectra in Sect. 5.2.2.3.1 we derived the linearity of the system, i.e. the peak position as a function of energy (shown in Figure 11), and the energy resolution, defined as the ratio between the Full Width at Half Maximum (FWHM) of each line and the peak position (shown in Figure 12).

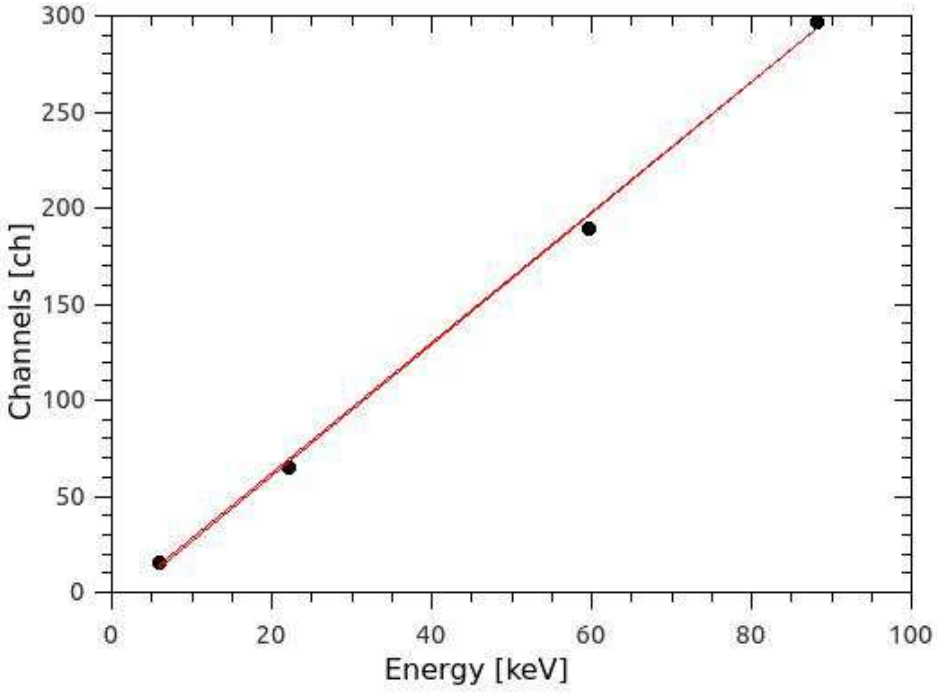

Figure 11: Linearity of the system of GAGG rod (3 mm × 3 mm × 30 mm) and LCT5 SiPM (nominal overvoltage of +3 V).

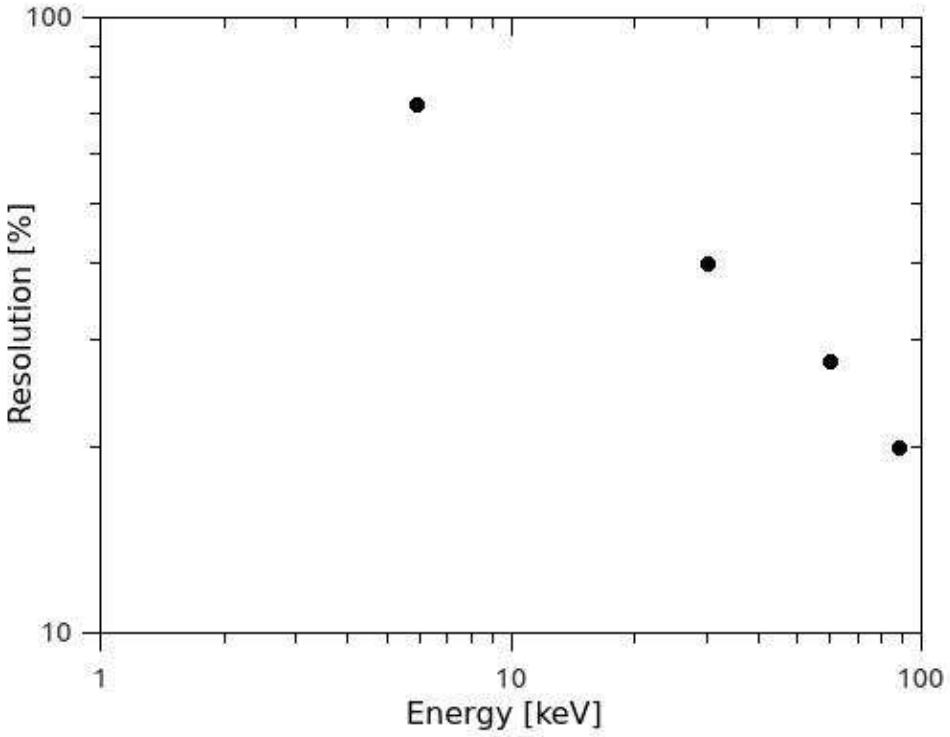

Figure 12: Energy resolution of the system of GAGG rod (3 mm × 3 mm × 30 mm) and LCT5 SiPM as a function of the energy. The energy resolution is defined as the ratio between the FWHM and the peak position.

5.2.2.3.3 Optimisation of the signal shape

To select the configuration of the Research Amplifier Ortec 450, we acquired the spectrum of the X-ray lines at 22.0 and 24.9 keV from ^{109}Cd and at 59.5 keV from ^{241}Am by testing various combinations of integration time (between 0.1 μs and 1 μs) and gain. For this characterisation we use the Multichannel Analyser Amptek MCA 8000A, which accepts input signals with minimum peaking time of 0.25 μs and has two dynamic ranges. We verified that the output signal from the Research Amplifier was not in pile-up by checking the symmetry of the spectrum and we measured the energy resolution. We found the best energy resolution for an integration time of 0.25 μs (see Figure 9) and, for this reason, we select 0.25 μs as the integration time of the Research Amplifier Ortec 450.

In addition, we tested different values of the SiPM overvoltage, between +1.5 V and +6.0 V. As an example, we show for the 59.5 keV line of the 241Am the position of the peak in the spectrum as a function of the overvoltage in Figure 13 and the energy resolution as a function of the overvoltage in Figure 14.

The performances of the absorbing stage are published in Ref. [9].

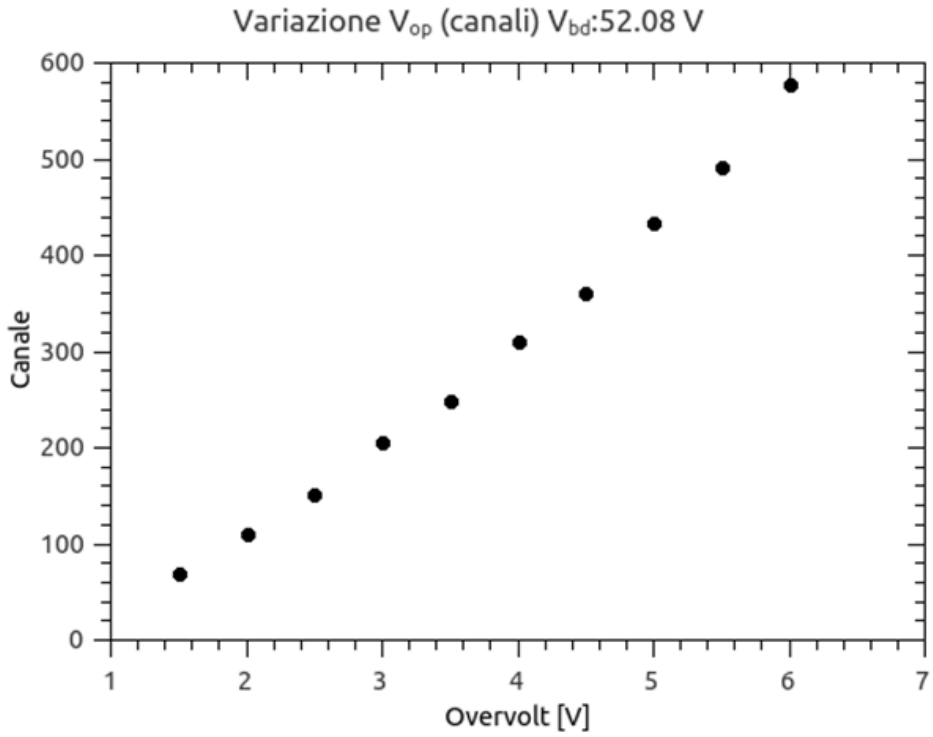

Figure 13: Position of the peak of the 59.5 keV line from ^{241}Am as a function of the Overvoltage

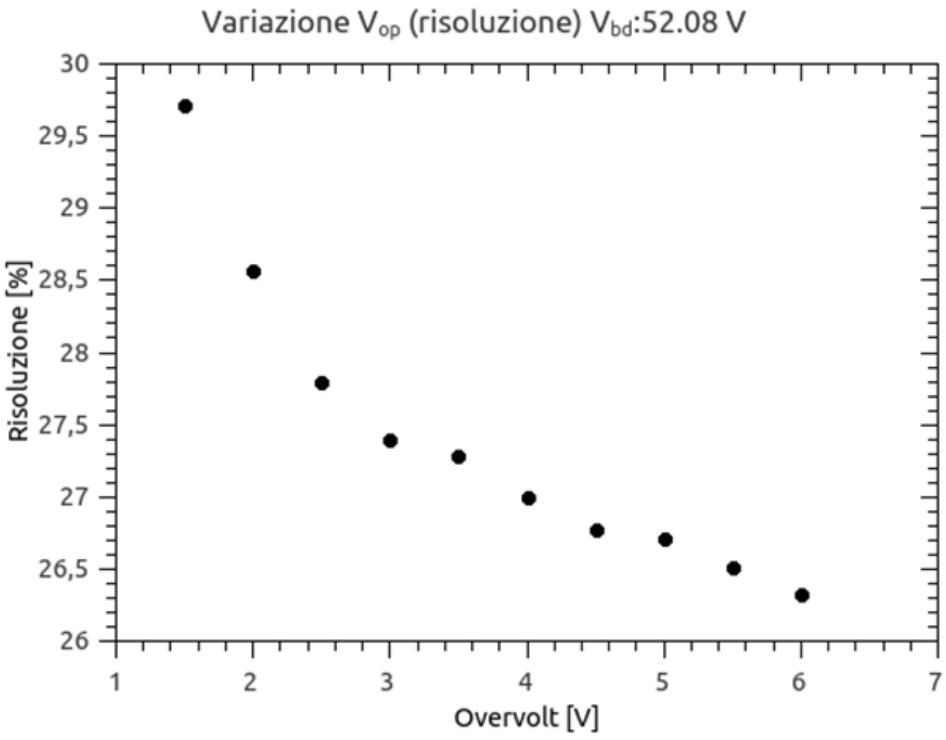

Figure 14: Energy resolution of the 59.5 keV line from ^{241}Am as a function of the Overvoltage

5.2.3 Characterisation with organic (plastic) scintillators

5.2.3.1 Scientific goals

The COMPASS design is based on “active” scattering elements, which are in charge of detecting the energy released in the scattering stage and giving the trigger. For example, a photon of 20 keV

Compton scattered at 90° deposits only 0.8 keV in the scattering stage. This is the order of magnitude of the energy on which the scattering stage is required to trigger. For this reason, the lower energy threshold of the scattering stage affects the lower energy threshold of the whole polarimeter.

Two parameters affect the lower energy threshold of the scattering stage: the light yield and the dark current rate. The amplitude of the output signal from the SiPM is given by the number of scintillation photons detected by the SiPM, in turn given by the product of the scintillator light yield (~10 photons / keV in the plastic scintillator) and the SiPM quantum efficiency (between ~30 % and ~40 % in the wavelength band of the scintillator emission). The wrapping of the scintillator rod impacts on the signal amplitude by affecting the number of scintillation photons reaching the entrance window of the SIPM. The dark current rate, produced by thermal excitation in the SiPM microcells**,** produces spurious signals even without the detection of scintillation photons.

Given the rates of this dark current (typically much higher than the equivalent rates in glass PMTs) the probability of chance coincidences is not negligible. On the other side the spectra of celestial sources are, in most cases, increase at decreasing energies. These are the two main ingredients for trade-off on the band.

5.2.3.2 Objectives and experimental set-up

In this section we report about the measurement of the dark current rate and the light yield for different types of scintillators proposed for the scattering stage, at different values of the SiPM overvoltage. In this characterisation we used the C12332 driving circuit and the internal preamplifier with an enhanced gain of 100. We connected the C12332 circuit to an electronic chain composed of the Timing Filter Ortec 474 (with integration time of 50 ns and differentiation time of 150 μs) and the multichannel analyser Amptek MCA 8000A. A block diagram of the experimental set-up is shown in Figure 15.

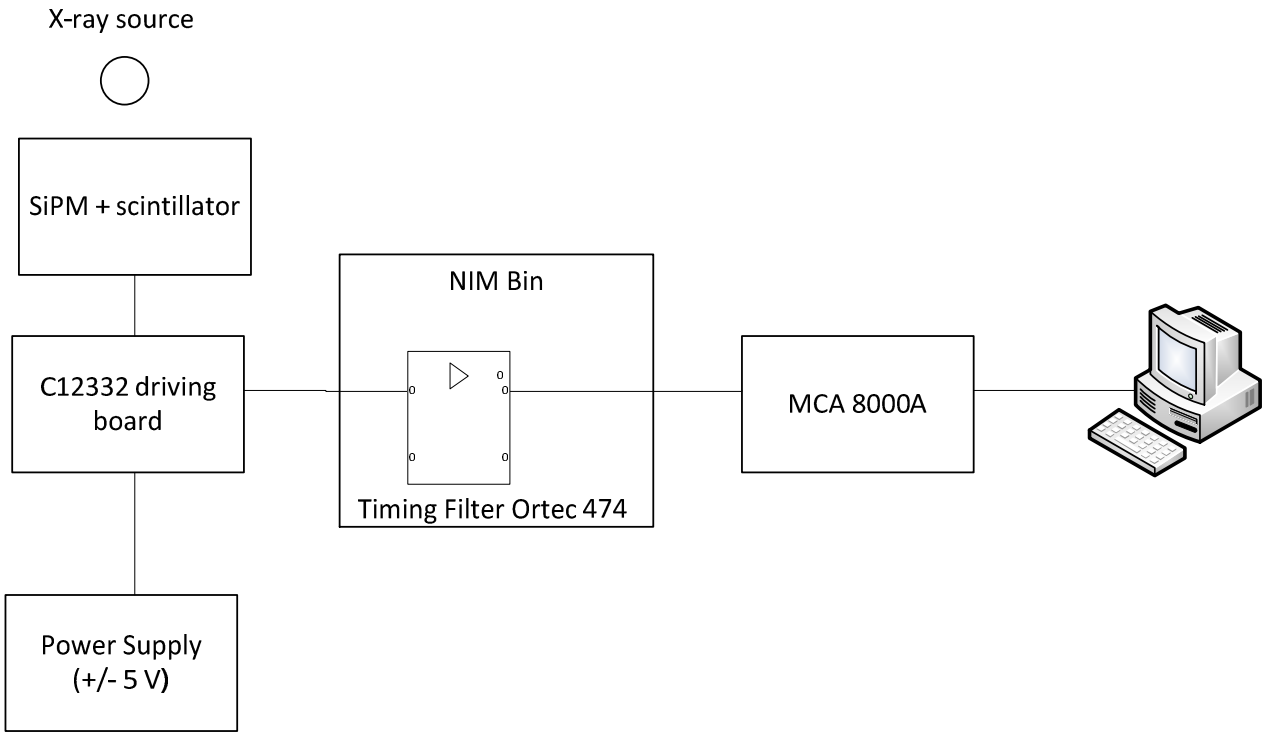

Figure 15: Block diagram of the experimental set-up

5.2.3.3 Results

5.2.3.3.1 The dark current rate

Compared to PMTs, SiPMs show a much higher dark current rate, e.g. of the order of 10^5 cts / s / electron (LCT5 SiPM with 50 µm pitch). As an example we show in Figure 16 the spectrum of the dark current rate measured at room temperature (~22 – 25 °C) without scintillator from an LCT5 SiPM with pitch of 50 µm and overvoltage of +3 V. After calibrating the ADC channels into charge, we derived the dark current rate from the integral of the spectrum from the maximum of the first electron peak up to the maximum of the fourth electron peak (represented by the gray area in Figure 17). The value of the integral for different values of the overvoltage is shown in Figure 18.

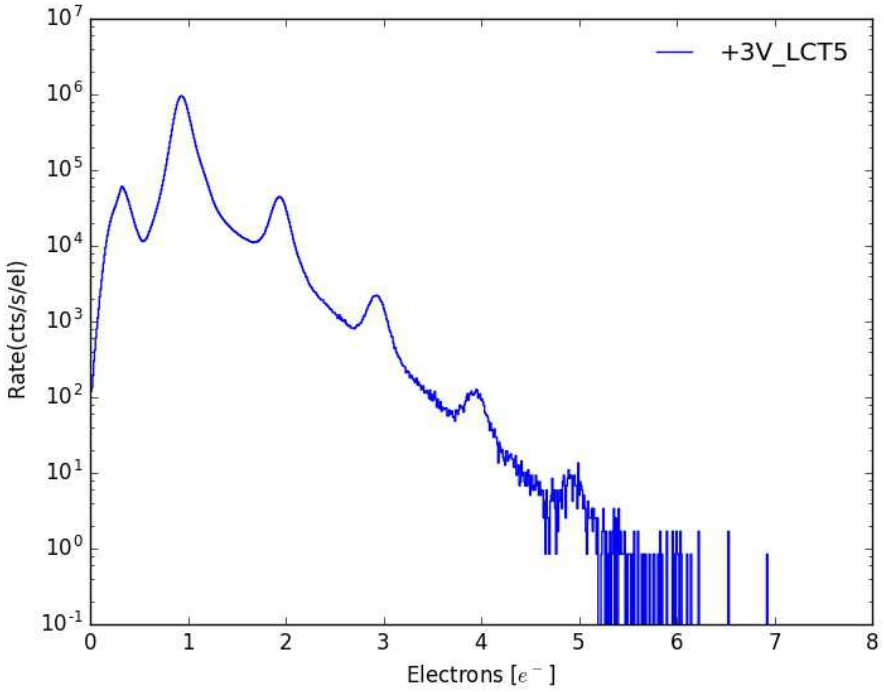

Figure 16: Spectrum of the dark current rate at room temperature (~22 - 25 °C) from an LCT5 SiPM with pitch of 50 µm and overvoltage of +3 V.

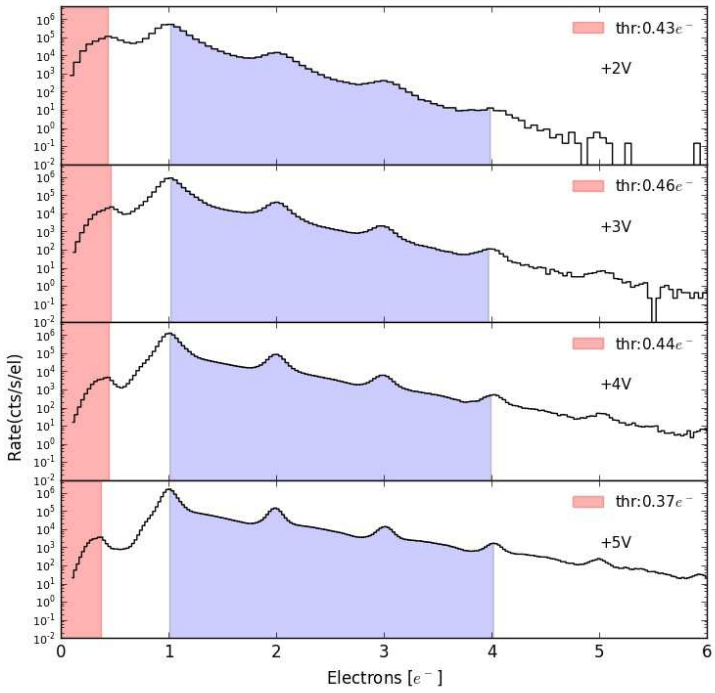

Figure 17: Integral of the spectrum of the dark current rate from an LCT5 SiPM with pitch of 50 µm at different values of the overvoltage (from +2 V to +5 V). The gray area indicates the region of the spectrum considered in the integral.

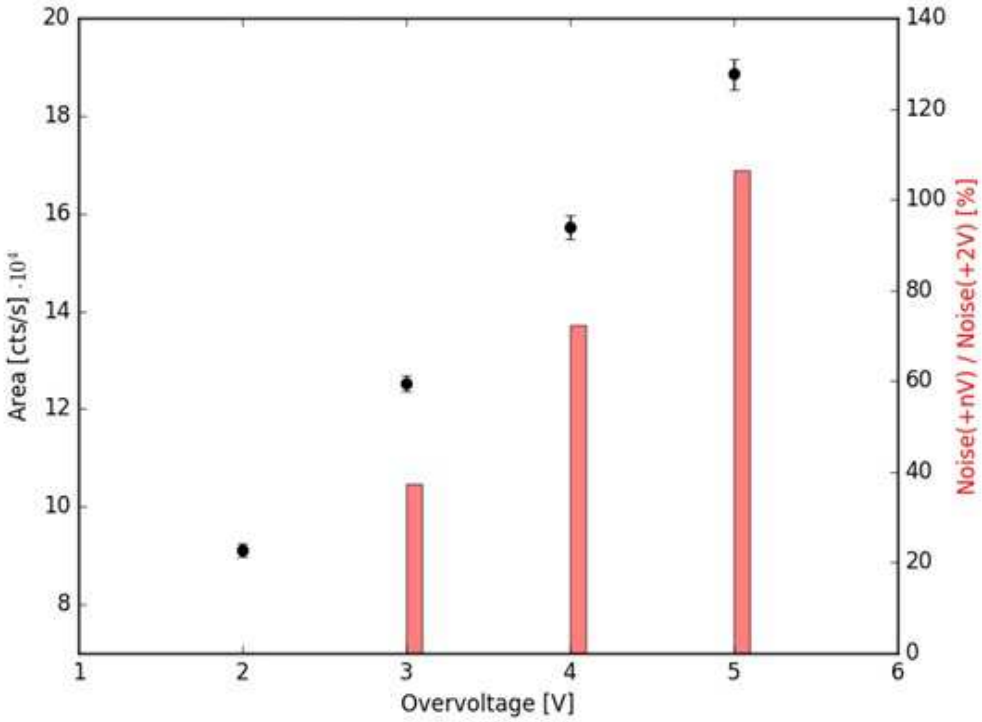

Figure 18: Integral of the dark current rate for different values of the overvoltage in an LCT5 SiPM with 50 µm pitch.

We can see from Figure 18 that the dark current rate increases of about a factor of two for an overvoltage increase of 1 V.

5.2.3.3.2 The light yield

We measured the light yield of the three types of plastic scintillator (EJ-204, EJ-200 and EJ-260) using the 22 – 24 keV line of a ^{109}Cd source. The scintillator rods are all wrapped with PTFE tape and connected to the same SiPM (LCT5 with 50 μm pitch).

An example of the spectrum accumulated with EJ-204 at the default overvoltage of +3 V is shown in Figure 19. The spectrum is composed of the sum of "narrow peaks", produced by the amplitude of the signal from individual pixels simultaneously triggering. In particular, Figure 19 shows the "narrow peaks" from 5 to 25 pixels simultaneously triggering. We modeled the whole spectrum as the sum of many gaussians, each one corresponding to a "narrow peak" and separately fitted. In Rosado and Hidalgo (2015) we find that the FWHM of each gaussian is proportional to √N (where N is the ordinal number of the gaussian), corresponding to the number of pixels simultaneously triggering. Then we fitted with a gaussian the distribution of the area of these "narrow peaks" to find the parameters of the spectrum of the 22 – 24 keV line, summarised in Table 1 for the different plastic scintillators at overvoltage of +3 V.

Table 1: Results of the fit of the spectrum of the 22 – 24 keV line from a ^{109}Cd source for the different plastic scintillators at the overvoltage of +3 V. All the scintillators are wrapped with PTFE tape.

Scatterer	Peak position [electrons]	Total rate [cts / s]	FWHM [electrons]	Light yield [e^- / keV]
EJ-200	12.8 ± 0.1	240 ± 5	10.4 ± 0.3	0.582 ± 0.005
EJ-204	13.03 ± 0.04	227 ± 2	10.1 ± 0.1	0.592 ± 0.002
EJ-260	14.29 ± 0.06	234 ± 3	11.2 ± 0.1	0.650 ± 0.003

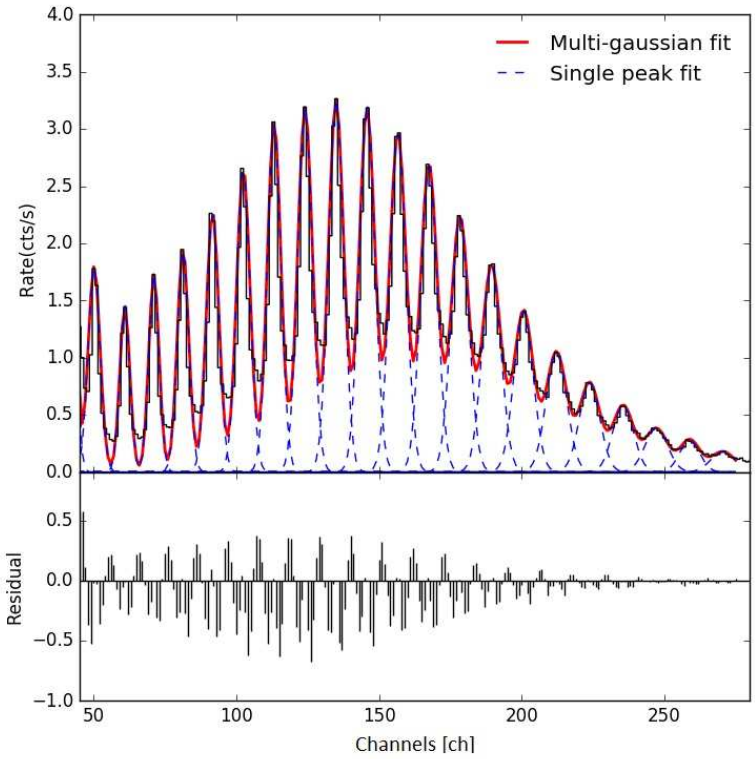

Figure 19: Example of the spectrum of the 22 keV line of 109Cd accumulated with EJ-204 at the default overvoltage of +3 V. Each "narrow peak" is separately fitted. The residuals are due to asymmetries introduced in the peaks by the electronic processing chain.

Assuming to use for the scattering stage the EJ-260, which has the highest measured light yield from the data in Table 1 (0.65 electrons / keV), we expect that an energy deposit of 0.8 would produce an average of 0.5 electrons. From the dark current rate in Figure 18, we expect at 0.5 electrons a dark current rate between ~10^4 and ~10^5 cts / s / electron.

5.2.3.4 Selection of the wrapping material to optimise the light yield

By replacing the wrapping of the EJ-260 rod with VM2000 reflecting paper instead of PTFE tape, we measured with the same source a light yield of 0.93 e^- / keV. The wrapping with VM2000 increases the light yield of 43 % with respect to the PTFE tape (see Figure 20).

The results of the characterisation of the scattering stage are published in Ref. [9].

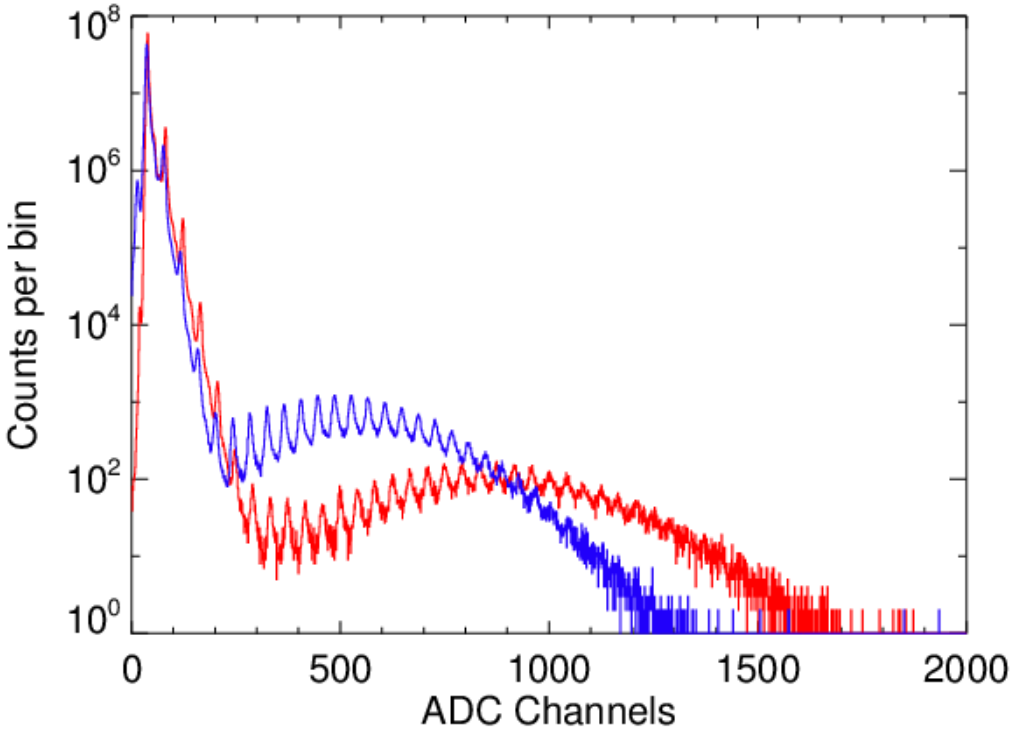

Figure 20: Superposition of the spectra of ^{109}Cd on EJ-200 with two different types of wrapping: PTFE tape (blue) and VM2000 (red). The two spectra have the same acquisition time of 1800 s.

5.3 Measurement of the photon-tagging efficiency

5.3.1 Scientific goals

As shown in Figure 1, for an X-ray polarimeter based on the Compton Effect, the modulation factor, i.e. the modulation in the count for a beam of 100% polarized X-rays with no background, is maximum for a scattering angle of 90° (see [5]). As written in Sec. 5.2.2 above, for a scattering angle of 90° the largest fraction of the X-ray energy is deposited in the absorber, while only a small fraction goes in the scatterer. For example for a Compton scattering angle of 90°, the energy deposited in the scatterer is 0.8 keV for an incident photon of 20 keV, 4.5 keV for 50 keV and 16.4 keV at 100 keV (see Figure 21). Consequently, the lower energy threshold of the whole polarimeter critically depends on the efficiency to detect low energy Compton electrons in the scattering stage after a Compton scattered photon is detected in the absorber. Hereafter we define this capability "photon-tagging efficiency in coincidence".

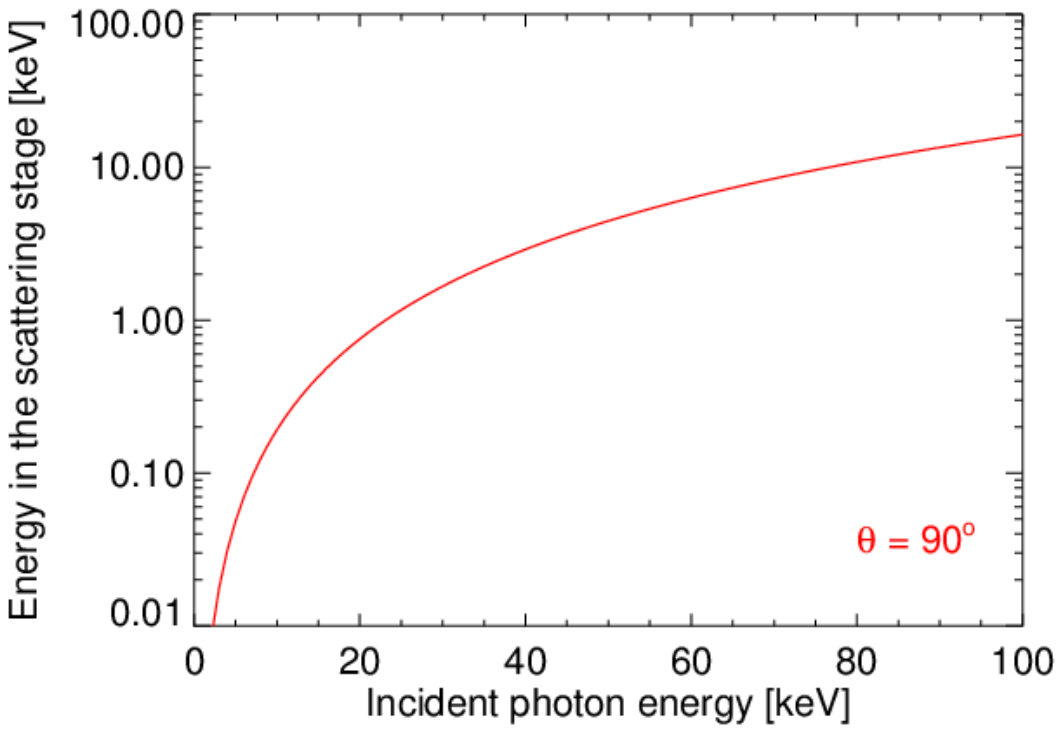

Figure 21: Energy deposited in the scattering stage for a Compton scattering at 90°

Fabiani et al. (2013) in Ref. [5] measured the photon tagging efficiency in coincidence using different types of scintillators for the scatterer, read-out using a vacuum PMT with enhanced quantum efficiency. This corresponds more or less to the best that can be done with conventional techniques. In this section we report about the measurement of the photon tagging efficiency in coincidence using for the scattering stage one rod of plastic scintillator and a SiPM (connected to the C12332 board).

5.3.2 Measurement method

As in Ref. [5], the photon tagging efficiency is defined as

$$\varepsilon_{tagging} = \frac{(R_{coinc} - R_{coinc\_rnd})}{(R_{tot} - R_{bkg})}$$

where

R_coinc is the rate measured in coincidence;

R_coinc_rnd is the rate of random coincidences;

R_tot is the total rate measured by the absorber in the same amplitude window without coincidence;

R_bkg is the background rate measured by the absorber in the same amplitude window without coincidence, i.e. with the X-ray source but without the plastic scintillator rod;

5.3.3 Experimental set-up

5.3.3.1 Instrumentation purchased to develop this experimental set-up:

- Newport stages
  - Optical Breadboard, 750 × 750 mm, 25 mm M6 Grid

    - 2 High Load Lab Jacks
    - 2 Precision Optical Rails
- Custom structure to hold the SiPM and the scintillator rod during the test, designed by us and produced by ISOLCERAM
- Ortec 4006 Minibin and Power Supply
- NIM module Ortec 850 Single Channel Analyzer
- Refurbishment of QUAD Scaler Ortec 976

5.3.3.2 Description of the experimental set-up

Each SiPM needs a complete C12332 driving circuit to work. We designed and manufactured a mechanical support structure to hold two SiPMs and the corresponding driving circuits at 90°. Due to the size of the sensor boards, this is the configuration to set the GAGG scintillator nearest to the plastic scintillator rod. Nevertheless, in this configuration the collecting area of the GAGG is only 9 mm^2 and the expected counting rate at the absorber is extremely low to be practically useful. For this reason, we decided to use as absorbing stage the Brillance 380 detector[2], already available in the IAPS laboratory. Brillance 380 is produced by Saint Gobain and is composed of a LaBr3 crystal (enclosed in metal housing with Be window) of 2.5 cm diameter and 2.5 mm thickness, integrated to a Hamamatsu R-3998-100-02 PMT. The collecting area of the Brillance 380 is 507 mm^2 and the solid angle is similar for the two configurations. Since the photon-tagging efficiency is measured for the scattering stage and the integration time depends on the area of the absorber, we select the Brillance 380 as the absorber in this measurement.

A picture of the experimental set-up is shown in Figure 22, a block diagram of the experimental set-up is shown in Figure 23.

The scattering stage is composed of a single rod of plastic scintillator from the list in Sec. 3 and a SiPM S13360-3050CS connected to a C12332 board with gain of 100. We use for the SiPM overvoltage the default value of +3 V. The scintillator rod is fixed on the SiPM entrance window using a drop of optical grease for scintillators. To improve the light yield, we put PTFE tape around the SiPM after fixing the scintillator. As in Figure 23, the output signal from the C12332 board is amplified using a Timing Filter Ortec 474 with an integration time constant of 50 ns and a differentiation time constant of 150 µs. The shaped signal is then provided to a QUAD SCA Ortec 850 with variable lower and upper thresholds. The logic output signal from the QUAD SCA is delayed of 0.166 µs using a Timing SCA Ortec 551 and is provided to the Coincidence module Canberra 2144A.

The output signal from the Brillance 380 is amplified using a PREAM-AMP-SCA Ortec 4890. The logic signal from the SCA section is provided to the coincidence module (Canberra 2144A). Both logic signals from the SCA of the scattering and absorption stages have a width of 0.5 µs. The coincidence window has consequently a width of 1 µs following the definition in Ref. [12].

The output signal from the coincidence module has a width of 1.6 µs and is fed to both a Scaler CAEN N145 and to the coincidence gate of the multichannel MCA 8000A that is used to record the counting rate. We measured for the MCA 8000A an efficiency of 100 % in recording the counting rate by comparing with the Scaler CAEN N145.

[2] Model 25 SBE 2.5 with Hamamatsu PMT model R 3998-100-02

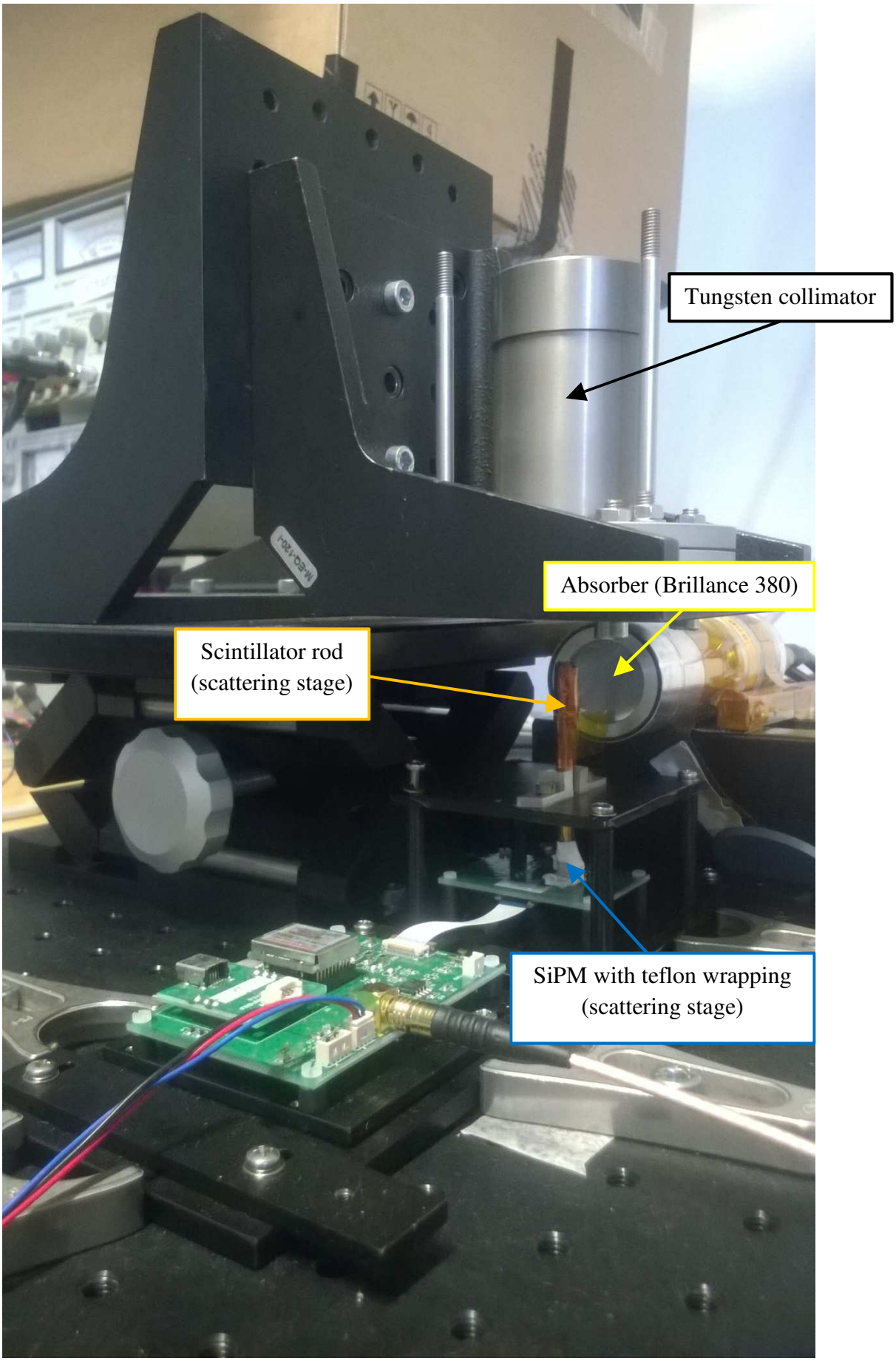

Figure 22: Picture of the experimental set-up

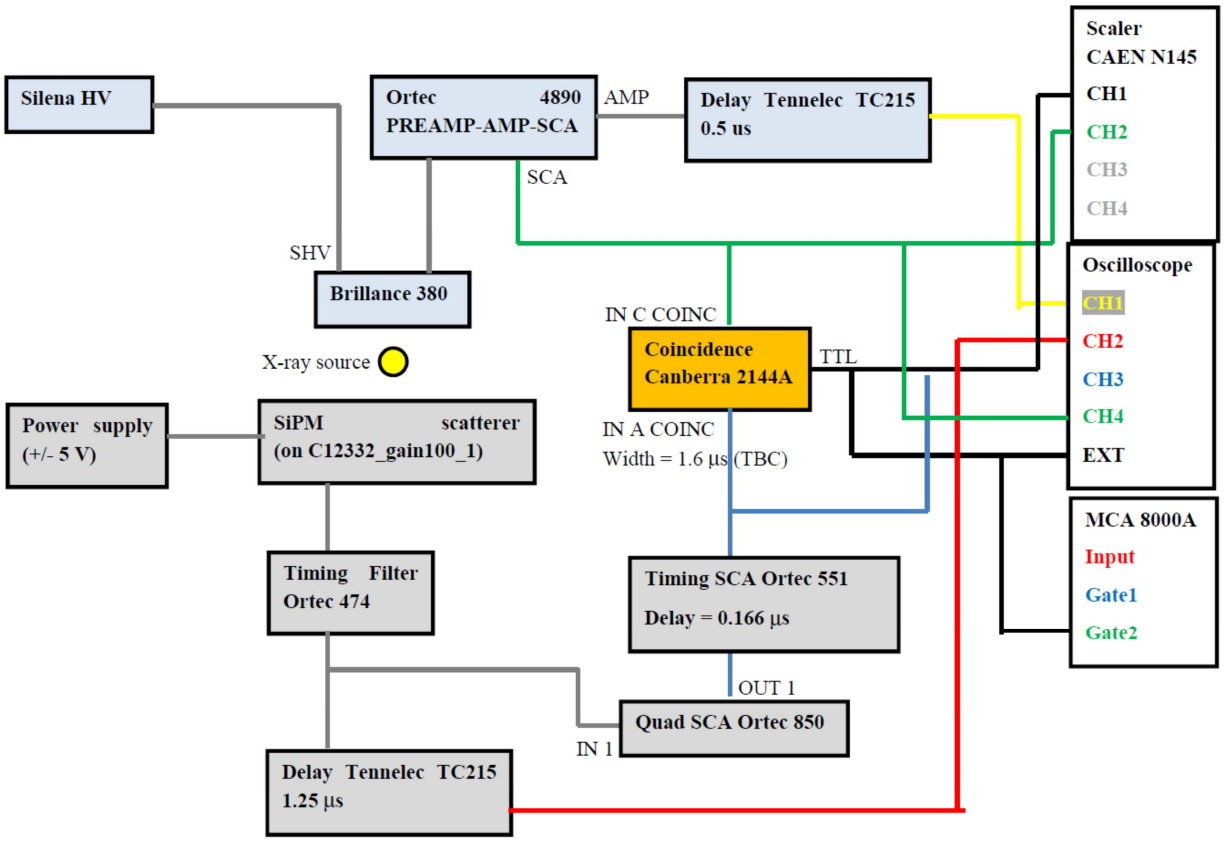

Figure 23: Block diagram of the experimental set-up

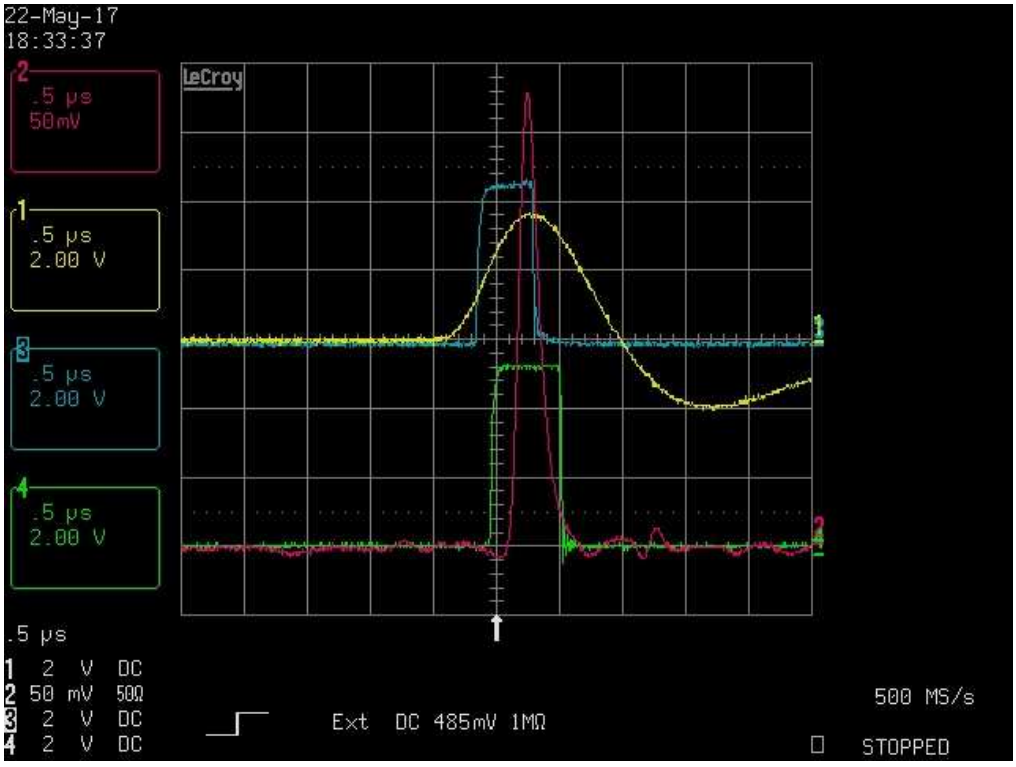

Figure 24: Oscilloscope screenshot with the following signals: CH1 (yellow): output from Ortec 4890 (Brillance 380) after delay of 0.5 µs; CH2 (magenta): Ortec 474 (SiPM) after delay of 1.25 µs; CH3 (cyan): SCA of Ortec 4890 (Brillance 380); CH4 (green): SCA of Ortec 850 (SiPM);

We measured the photon tagging efficiency at two energies: 22 keV (from a ^{109}Cd source with ~650 µCi activity) and 59.5 keV (from ^{241}Am with ~10 µCi activity). The measurement was performed with one source at a time. During the measurement, the source is enclosed in a collimator made of Tungsten (see Figure 22), used to reduce the background. The source is collimated using two diaphragms of ~4 mm aperture at ~5.5 cm distance.

5.3.4 Results

We show the results of the measurement of the photon tagging efficiency in Table 2.

Table 2: Results of the measurement of the photon tagging efficiency $\varepsilon_{tagging}$, calculated as defined in Sec. 5.3.2.

Source	Energy [keV]	Absorber	Scatterer	$\varepsilon_{tagging}$ [%]	$\sigma(\varepsilon_{tagging})$ [%]
^{241}Am	59.5	Brillance 380	EJ-200 + VM2000	67.3	1.6
^{241}Am	59.5	Brillance 380	EJ-260 + VM2000	51.2	2.2
^{109}Cd	22.0, 24.9	Brillance 380	EJ-260 + VM2000	14.6	0.3

The threshold is 0.04 V, corresponding to 0.3 e^-. All plastic scintillators have 6 cm length and are wrapped using VM2000 reflective paper, which provides the highest light yield for the plastic scintillator and is the baseline for this type of measurements.

5.3.5 Discussion

The scattering stage composed of a plastic scintillator rod (6 cm height and 3 mm side) with a SiPM can tag photons of ~0.8 keV energy with an efficiency of ~15 %. It is worth noting here that we compute the photon tagging efficiency by subtracting the chance coincidence rate, due to the dark current rate of the SiPM. Consequently, the dark current rate is not affecting the measurement.

In addition, the maximum measured rate is of the order of ~30 cts / s and is more than three orders of magnitude below the maximum rate (~200000 cts / s by the MCA 8000A) that can be processed by the acquisition chain in Figure 15.

Fabiani et al. (2013) [5] measured with a similar technique the photon tagging efficiency of a plastic scintillator (BC-404 by Saint-Gobain, 5 mm diameter and 3 cm height) and an organic scintillator (p-terphenyl of 7 mm diameter and 3 cm height) using a PMT as readout element. in addition, they measured the tagging efficiency for different wrapping materials for both the plastic scintillator and the p-terphenyl.

At 59.5 keV, Fabiani et al. (2013) [5] found an efficiency of 87.1 % for p-terphenyl (7 mm diameter and 3 cm height). This value is compared to 67.3 % for EJ-200 and 51.2 % for EJ-260.

At 22 keV, we measured an efficiency of 14.6 % with EJ-260 while Fabiani et al. (2013) [5] range from 36.3 % for BC-404 with VM2000 wrapping to 47.5 % for p-terphenyl with TETRATEX wrapping.

The photon tagging efficiency measured with this experimental set-up is generally lower than measured in Ref. [5]. A likely contribution to this difference are the different dimensions of the scintillator in the scattering stage. For example, we show in Figure 25 the fraction between the

photopeak position and the position at 15 mm height measured as a function of height on a plastic scintillator rod (EJ-204) with 3 mm × 3 mm × 10 cm size. The measurement has been performed in our laboratory using a Hamamatsu H10721-110 PMT-sel PMT. The scintillator rod was coupled to the PMT entrance window with a drop of optical grease, the same system used to couple the scintillator rod on SiPMs.

The variation of the photopeak position is proportional to the light yield of the scintillator, thus the plot in Figure 25 shows how the geometry of the scintillator rod affects the light yield at the base. This is a possible explanation of the smaller photon tagging efficiency than measured in Ref. [5]. In fact, the scintillator rods in Ref. [5] have a more favorable geometry (5 mm diameter and 3 cm length) than in our measurements (higher length of 6 cm and smaller side of 3 mm).

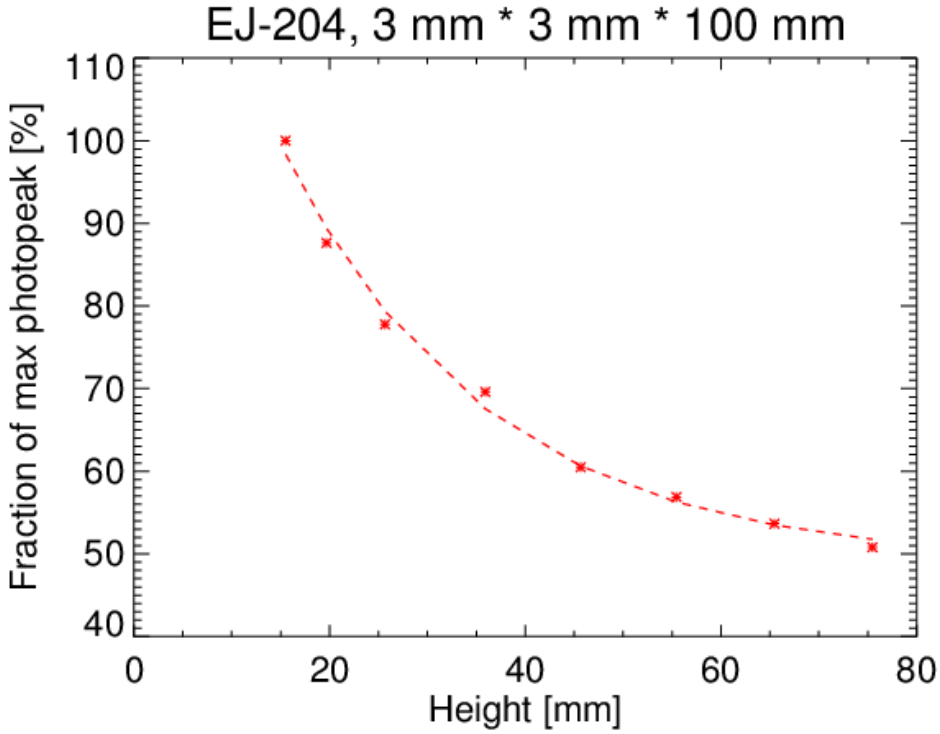

Figure 25: Fraction of the photopeak position as a function of height for a plastic scintillator rod of EJ-2014 with 3 mm × 3 mm × 10 cm size. The height is measured from the PMT entrance window. The minimum height is 15 mm and is due to the experimental set-up.

5.4 Characterisation of the CITIROC ASIC as front-end electronics for SiPMs

The above testing activity is based on devices off the shelf from Hamamatsu. An actual experiment of X-ray polarimetry will require a much larger number of pixels, a fine subdivision, while still preserving a good timing capability and a built in capability to perform coincidences. Before we arrive to develop a dedicated ASIC chip we have searched for existing devices that could allow for the transition from a testing activity based on 1 – 2, a few parts to a testing activity based on a ten or a few tens elements. In the search for an existing ASIC suited for this second stage of testing we considered experiments of physic research with similar requirements in terms of fine subdivision, rapidity, dynamics and so on.

In this sense an experiment of X-ray scattering polarimetry shares many commonalities with the focal plane of a Cherenkov telescope. Given the significant engagement of INAF in CTA we searched for potential share of existing technologies.

CITIROC is the Cherenkov Imaging Telescope Integrated Read Out Chip, the front-end chip of the camera for the ASTRI SST-2M, one of the prototypes for the small sized telescopes of the Cherenkov Telescope Array.

CITIROC, designed by WEEROC, is based on the extended analogue Silicon photo-multiplier integrated read out chip (EASIROC) architecture (see references [14][15][16][17][18]), with the addition of the custom functions required by the ASTRI team.

CITIROC is a 32 channel fully analog front-end ASIC designed to read out SiPMs with sensitivity at level of single photon electron. Its analog core and characteristics are listed in [19]. The processing of the analog signal takes place in the front-end channels of the device, while the read out is handled at the internal back-end of the ASIC.

A schematic view of CITIROC design is shown in Figure 26. Two separate electronics chains allow for High and Low-gain (HG and LG) simultaneous processing of the analog signal. Each of the two chains is composed of an adjustable preamplifier followed by a tunable shaper (SSH: Slow Shaper), and a selectable track-and-hold circuit (SCA: Switched Capacitor Array) and an active Peak Detector (PD) employed to capture and hold the maximum value of analog signal. Fine-tuning of each pixel gain is obtained adjusting the voltage applied to the SiPM through an 8-bit Digital-to-Analog Converter (DAC) ranging from 0 to 4.5 V. A third chain implements the trigger channel generation using a fast shaper (FSB: Fast Shaper Bipolar) with fixed shaping time of 15 ns, followed by two discriminators.

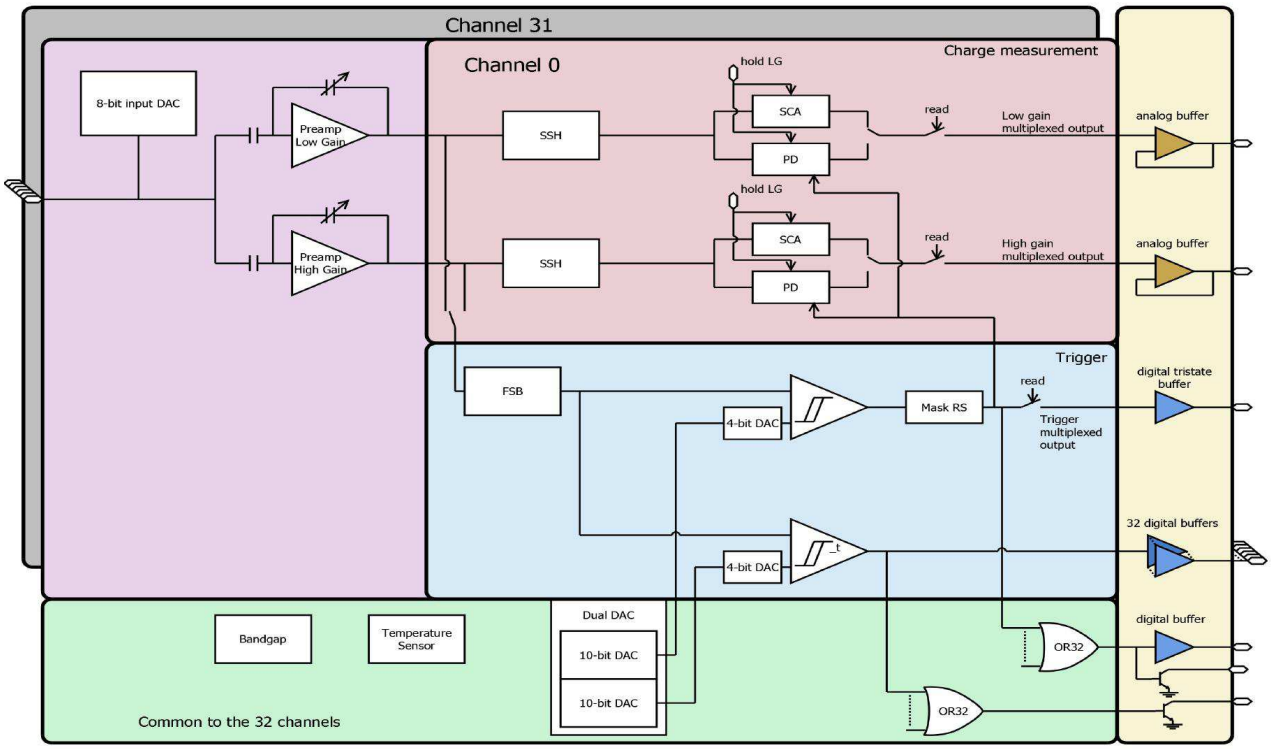

Figure 26: Architecture of the CITIROC ASIC

5.4.1 Scientific goals

The goal of this activity is focused on the characterization of the CITIROC ASIC for the readout of SiPMs coupled to scintillators for Compton polarimetry. An experimental set-up has been designed to operate the CITIROC ASIC mounted on the evaluation board provided by WEEROC. The set-up

allows to perform measurements by operating the evaluation board via PC and keeping the SiPM at stable and controlled temperature by means of a Peltier device.

5.4.2 Experimental set-up

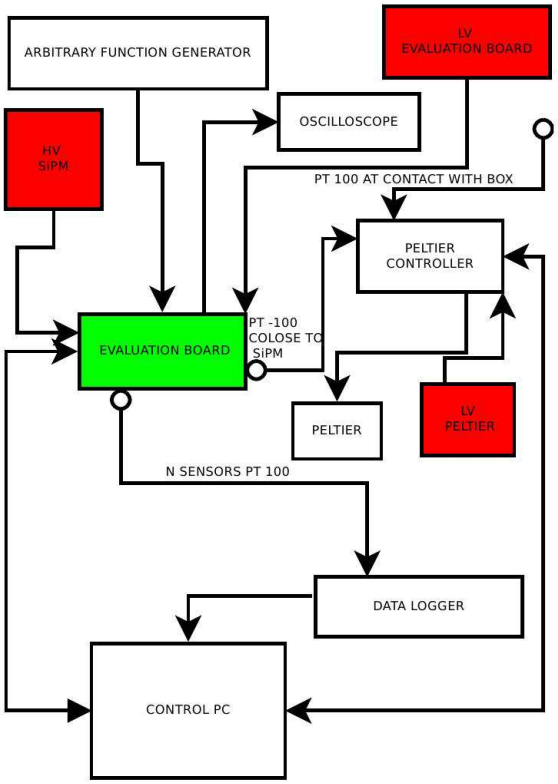

Figure 27: Block diagram of the experimental set-up

The experimental set-up includes the items shown in the block diagram of Figure 27. The evaluation board of the CITIROC ASIC (see Figure 28) is powered with a low voltage line at 6.5 V and a high voltage line at about 60 V for the SiPM. A box made of anticorodal allows for creating a light-tight environment and electromagnetic shield. A scintillating bar can be placed on the top of the SiPM to readout the light signal. To maintain the alignment and the optical contact between the SiPM and the scintillating bar and the alignment between the bar and the X-ray beam exiting from a collimator / source holder made of tungsten, a custom made structure was designed. This structure is sustained by means of a board on which also the SiPM is mounted (see Figure 29).

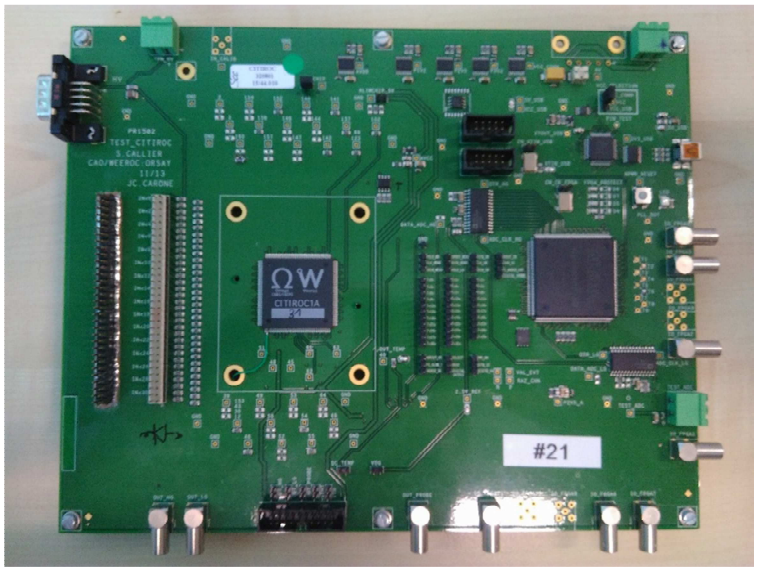

Figure 28: CITIROC ASIC evaluation board

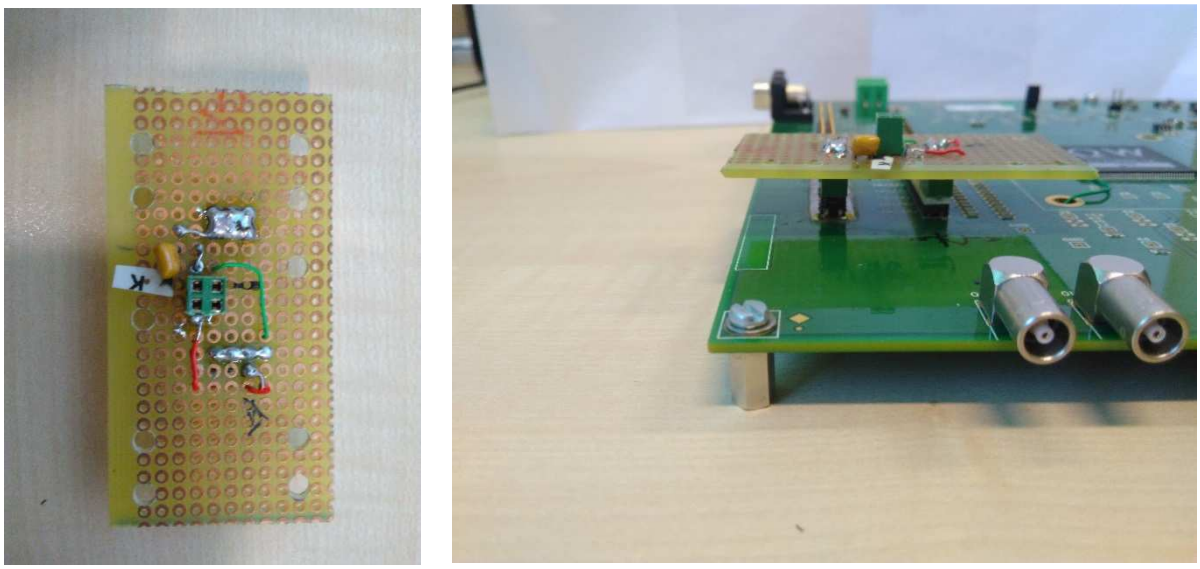

Figure 29: On the left: SiPM board. On the right: SiPM board mounted on the evaluation board of the CITIROC ASIC

The temperature in the light-tight box is regulated by means of a Peltier/controller assembly.

An arbitrary function generator can be connected to the test board when the SiPM is not connected and powered to allow the test of the electronic chain of the 32 channels all together.

Two analog outputs for the low gain and high gain chain allows to display the signal directly on the oscilloscope.

The digital signal from the evaluation board is read out by means of an USB cable connected to the control PC.

5.4.2.1 Instrumentation purchased to develop this experimental set-up:

- Digital oscilloscope Keysight MSOX3104T
- Peltier cooler with power supply and TC-XX-PR-59 programmable controller
- Programmable DC power supply TDK-Lambda Z+
- Frequency counter/timer Keysight 53230A
- Cables and connectors to equip the custom box;
- PC and monitor for the acquisition system;
- Multimeter Keysight 34465A
- Source Measurement Unit Keysight 6614C
- Tungsten collimator for the ASIC box, designed by us and produced by Tungsten Alloy
- Custom box to hold the CITIROC evaluation board during the test, designed by us and produced by the mechanical workshop at IAPS.

The light-tight box design is shown in Figure 30 in which also the Peltier assembly is shown mounted underneath the box. It comprises three sections: the main section in which the evaluation board is hosted, the flat cover and a cap that hosts the assembly of the X-ray source, the collimator and the scintillating bar shown in Figure 31. The box is equipped with two fast tube fittings to allow for a dry air flow of nitrogen. It is useful to prevent water vapor condensation in the box when cooling.

The box has a black anodized to allows parasitic light absorption. At the junction of the flat cover and the cap a rubber gasket is inserted to prevent the entering of stray light.

5.4.2.2 Custom designed box

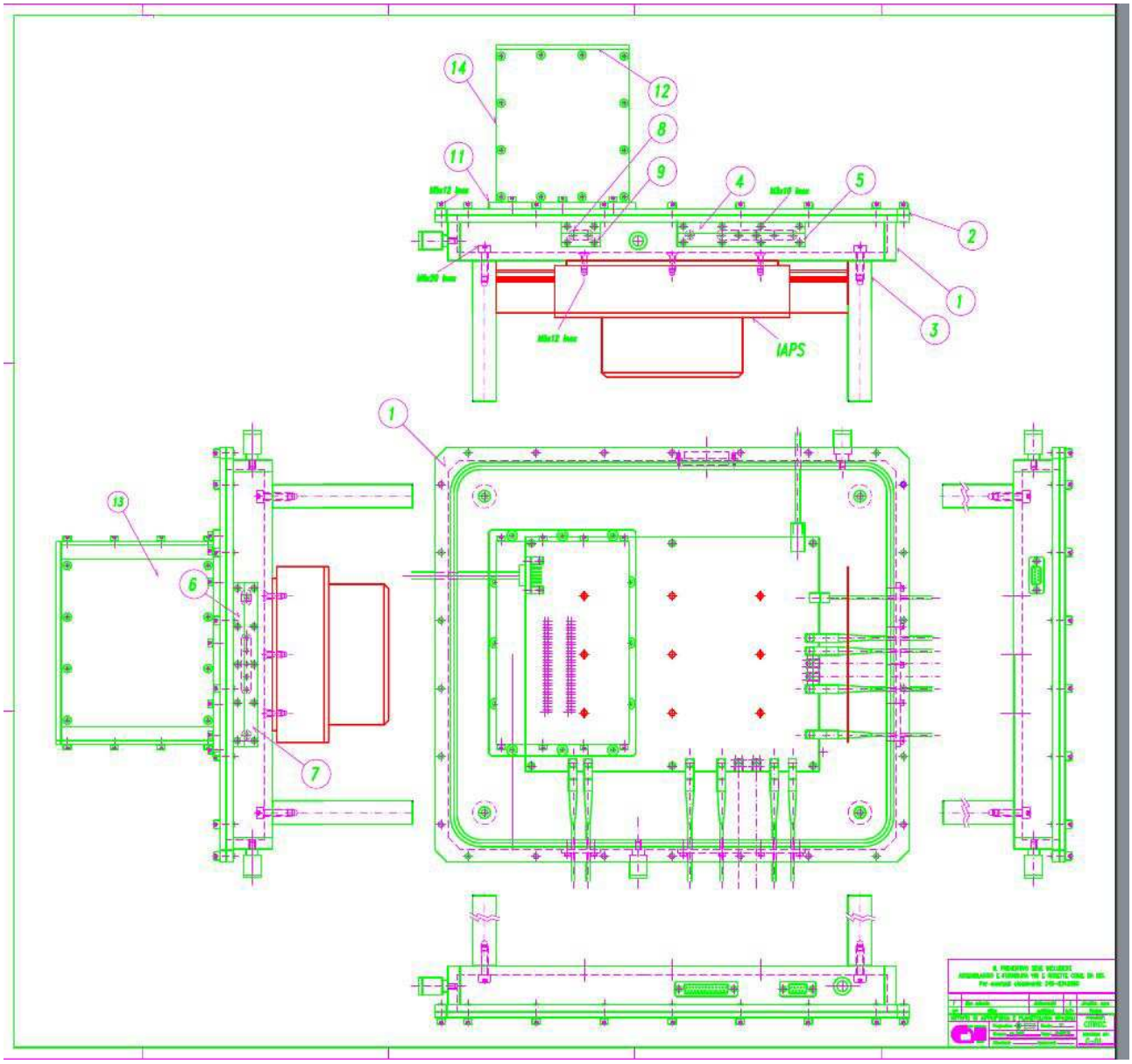

Figure 30: Custom designed box with Peltier assembly

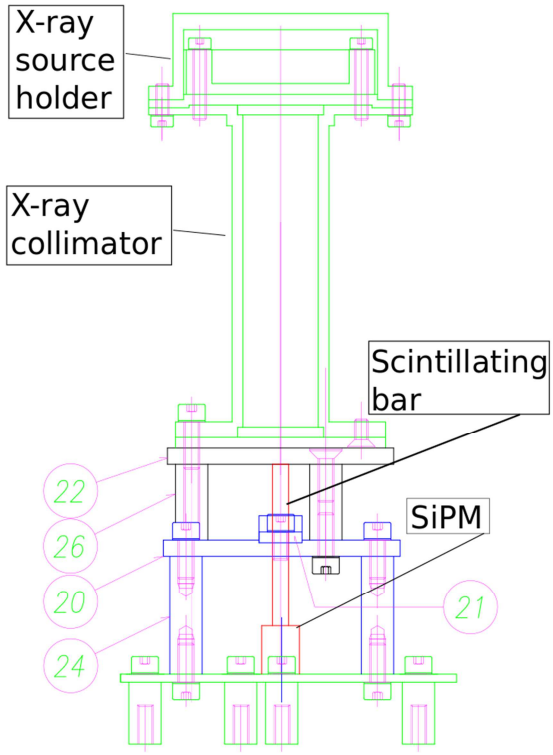

Figure 31: Assembly that holds the SiPM, the scintillating bar and the X-ray collimator with the source holder

5.4.2.3 Temperature regulation of the ASIC in the box

A Peltier direct-contact-to-air assembly (see Figure 32) allows to cool the box via conduction. Heat is absorbed through a cold plate, pumping the heat through the Peltier device dissipating it into the air through a heat sink equipped with fan and shroud. The aluminum cold plate is screwed underneath the box and the thermal contact is ensured by means of a thermal pad. The Peltier direct-contact-to-air assembly, powered with a low voltage independent line, is operated with a TC-XX-PR-59 programmable controller (see Figure 33). The unit allows for reversible (cooling/heating) control of the box temperature with high control accuracy. The controller not only regulates the temperature, but also features two programmable fan outputs and an alarm output relay. The controller can be used as a stand-alone unit with RS-232 interface to control settings and parameters live. An easy to use PC software is used to input parameters visually and see output parameters in real time. The box is padded with a thermal insulating layer to reduce convection and irradiation towards the surrounding environment. The Peltier controller needs at least two thermal sensors (PT-100) to monitor the temperature: one close to the SiPM to monitor the air temperature and one in contact with the box wall close to the cold plate. More thermal sensors connected to a data logger (connected to the PC) can be placed to monitor more accurately the temperature.

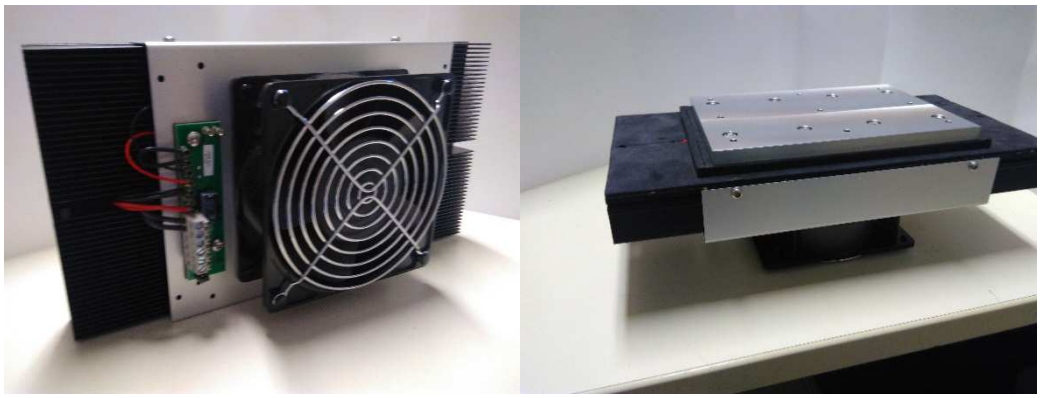

Figure 32: Peltier assembly

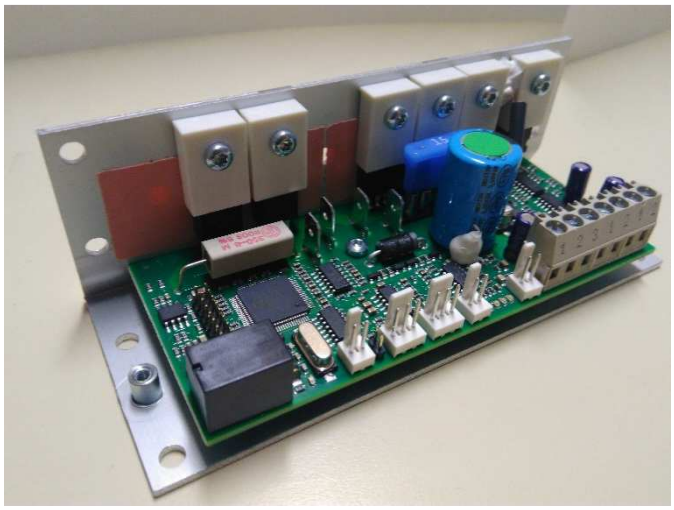

Figure 33: TC-XX-PR-59 programmable controller of the Peltier assembly

5.4.2.4 Customisation of the software

WEEROC provides the evaluation board of the CITIROC ASIC with a LabView software that allows for data acquisition. The original software performs real time data acquisition in such a way that a file for each event acquired (signal triggered) is saved in a directory. The files comprise, for each event, two columns. The first one reports the ASIC channel number from 0 to 32 (32 rows), the second one reports the corresponding ADC value measured (from 0 to 4095). Thus, at the end of a measurement session a number of files equal to the number of triggered events is saved on the PC hard drive. Moreover, if only the ASIC channel *k* is triggering the acquisitions, only the *k* row of the files corresponding to that channel will report an ADC value much higher with respect to the other ones. This operating mode overloads the PC due to the continuous access to the hard drive for writing files. We customized the software by adding a new operational mode that save on the hard drive only 32 files for a measurement session, one file for each ASIC channel (32 channels). These files comprise 4095 rows (ADC channels) which report the sum of the number of events that triggered for that specific ADC value. Therefore, the histogram of the energy spectrum in terms of ADC channels is directly saved in files for each one of the 32 ASIC channels during an acquisition.

We customized also the visual interface to properly display in real time energy spectra acquisition in this data acquisition mode.

5.4.3 Characterisation of the SIPM and CITIROC with a light stimulation

To characterize and calibrate the SiPMs, silicon light sensors, used in the COMPASS project we use as light stimulation, as well as the usual led driven by a function generator, a Laser System.

The Laser System acquired is the PicoQuant PDL 828 Sepia II.

The fundamental characteristics of this Laser System is that it can be controlled by computer, also remotely, and has the possibility to set a wide choice of spectral, temporal and power parameters. Moreover, its characteristics allow a convenience and flexibility of use also for the future as the system is expandable and modular. The system allows the complete control of the laser power and can operate both in impulsive and continuous mode with selectable wavelengths and with the possibility of adding other modules for specific functions.

The capabilities of the Laser System include the possibility to have pulses at frequency up to about 100 MHz. This is very important to characterize not only the SiPM but also the Front-End electronics based on the CITIROC Chip.

The PicoQuant PDL 828 Sepia II Laser System

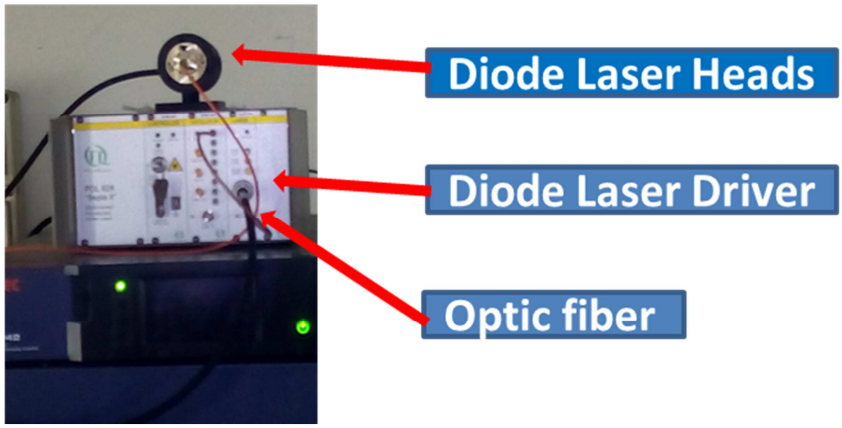

The Laser System inside the climatic chamber

5.4.3.1 Instrumentation purchased for this experimental set-up

- PicoQuant PDL 828 Sepia II.

5.5 Correlation methods for the analysis of X-ray polarimetric signals

The measurements of the X-ray polarisation are based on the study of the distribution of the directions of scattered photons or photoelectrons and on the search of a sinusoidal modulation with a period of π. This method is used for both photoelectric and Compton polarimeters.

An important issue in polarization measurements is the possibility to have a noise distribution differing from the Poissonian one because of intrinsic effects in the detection technique. For instance, in a photoelectric polarimeter as the GPD the uncertainty on the initial direction of the photoelectron can be influenced by the hexagonal geometrical pattern of pixel plane (especially for tracks comprising a very small number of pixels) producing a not uniform spread of angular directions in the phase histograms. Thus the assumption that the noise on the angular distribution is white and purely Poissonian cannot be always verified.

In the framework of the COMPASS project, we developed a new simple tool based on a scatter plot of the distribution histograms in which the frequency values are reported after a shifting by 1/4 of the period. In case of a linearly polarised emission, the sinusoidal pattern is transformed into a circular plot with radius equal to the amplitude of the modulation, while for an unpolarised radiation the scatter plot is reduced to a random point distribution centred at the mean frequency value. Our correlation methods are not based on the assumption of purely Poissonian noise and thus provide direct visual tools for evaluating the quality of polarization measurements and for investigating distortions due to systematic effects.

We published this innovative correlation method in a paper on the journal Nuclear Instruments and Methods in Physics Research A:

Enrico Massaro, Sergio Fabiani, Riccardo Campana, Enrico Costa, Ettore Del Monte, Fabio Muleri, Paolo Soffitta, “Correlation methods for the analysis of X-ray polarimetric signals”, Nuclear Instr. and Methods in Phys. Res. A, 885, 7 – 14 (2018)

We attach at the end of this document the published version of the paper.

5.6 Conclusions

We have shown in Sec. 5.2 that SiPMs are suitable read-out elements for scintillators of both high-Z as the GAGG and low-Z as the plastic scintillator.

We measured on the scattering stage a photon tagging efficiency of ~15 % (EJ-260) at 22 keV and ranging from ~51 % (EJ-260) to ~67 % (EJ-200) at 59.5 keV.

We designed and produced the experimental set-up, both hardware and software, to integrate a single SiPM with the CITIROC ASIC.

We submitted a paper to propose two simple tools for measuring the polarization parameters based on correlations between pairs of bins in the angular distribution having selected shifts. We verified with laboratory data and with numerical simulations that the results of the circular plot method are fully consistent with those obtained by means of Stokes' parameters, indicating that our estimator is unbiased. This method could be useful for the study of polarimetric data since it allows a fast determination of the polarization (degree and angle) and of the level of absence of spurious effects other than those that provide sinusoidal signal.

6 Future perspectives

We have shown in Sec. 5.3.4 the results of the photon tagging efficiency for two X-ray sources: ^{109}Cd, emitting the lines at 22.0 keV and 24.9 keV, and ^{241}Am, emitting a line at 59.5 keV. We plan to develop a Montecarlo simulation of the measurement with GEANT to estimate the efficiency at other energy. We can also measure the photon tagging efficiency at lower energy, e.g. using the 14 keV line of ^{57}Co, although we expect an efficiency lower than ~15 %, measured at 22.0 – 24.9 keV.

The photon tagging efficiency reported in Sec. 5.3.4 is the first measured with SiPMs as readout element for the scattering stage. Although the reported results are promising, we can perform various optimisations to increase the efficiency, e.g. by

- Increasing the light yield of the scintillator in the scattering stage by
  - selecting the organic or plastic scintillator with the highest light yield when coupled to the SiPM;
  - selecting the optimal wrapping material, i.e. giving the highest light yield;
  - finding the optimal geometry (height and size) of the scintillator rods, taking into account that SiPMs are a rapidly evolving technology and new models are produced every year;
- Optimising the SiPM overvoltage.

A front-end electronics based on an ASIC is necessary to design an instrument for a satellite or balloon mission. We have identified the CITIROC as a candidate ASIC for the Compton polarimeter. For this reason we plan to measure the photon tagging efficiency using the CITIROC ASIC as readout element for the SiPMs.

7 References

[1] M. C. Weisskopf, B. Ramsey, S. O'Dell, A. Tennant, R. Elsner, P. Soffitta, R. Bellazzini, E. Costa, J. Kolodziejczak, V. Kaspi, F. Muleri, H. Marshall, G. Matt, R. Romani, "The Imaging X-ray Polarimetry Explorer (IXPE)", Procs. SPIE, **9905**, 990517 (2016)

[2] E. Costa, P. Soffitta, R. Bellazzini, A. Brez, N. Lumb, G. Spandre, "An efficient photoelectric X-ray polarimeter for the study of black holes and neutron stars", Nature **411**, 662 (2001)

[3] M. Weisskopf, B. Ramsey, S. L. O'Dell, A. Tennant, R. Elsner, P. Soffitta, R. Bellazzini, E. Costa, J. Kolodziejczak, V. Kaspi, F. Mulieri, H. Marshall, G. Matt, R. Romani on behalf of the entire IXPE Team, "The Imaging X-ray Polarimetry Explorer (IXPE)", Results in Physics, **6**, 1179 – 1180 (2016)

[4] E. Costa, M.N. Cinti, M. Feroci, G. Matt, M. Rapisarda, "Design of a scattering polarimeter for hard X-ray astronomy", NIM A, **366**, 161 – 172 (1995)

[5] S. Fabiani, R. Campana, E. Costa, E. Del Monte, F. Muleri, A. Rubini, P. Soffitta, "Characterization of scatterers for an active focal plane Compton polarimeter", Astroparticle Physics, **44**, 91 – 101 (2013)

[6] D. Impiombato, S. Giarrusso, T. Mineo, O. Catalano, C. Gargano, G. La Rosa, F. Russo, G. Sottile, S. Billotta, G. Bonanno, S; Garozzo, A. Grillo, D. Marano, G. Romeo, "Characterization and performance of the ASIC (CITIROC) front-end of the ASTRI camera", Nuclear Inst. and Methods in Physics Research A, **794**, 185 – 192 (2015)

[7] Furukawa datasheet of GAGG crystals, available at https://furukawa-st.co.jp/doc/Ce_GAGG.pdf

[8] J. Iwanowska, L. Swiderski, T. Szczesniak, P. Sibczynski, M. Moszynski, M. Grodzicka, K. Kamada, K. Tsutsumi, Y. Usuki, T. Yanagida, A. Yoshikawa "Performance of cerium-doped Gd3Al2Ga3O12 (GAGG:Ce) scintillator in gamma-ray spectrometry" Nuclear Instruments and Methods in Physics Research A, **712**, 34 – 40 (2013)

[9] E. Del Monte, A. Rubini, A. Brandonisio, F. Muleri, P. Soffitta, E. Costa, G. Di Persio, S. Di Cosimo, E. Massaro, A. Morbidini, E. Morelli, L. Pacciani, S. Fabiani, D. Michilli, S. Giarrusso, O. Catalano, D. Impiombato, T. Mineo, G. Sottile, S. Billotta, "Silicon photomultipliers as readout elements for a Compton effect polarimeter: the COMPASS project", Procs. SPIE 9915, id. 991528 13 pp. (2016)

[10] Cucoanes A. S., "A Toy Model for the Gamma Spectrum Generated in n-Captures on Gd", http://www.yakkas.jp/DChooz/document/AndisFunction/Gd_cucoanes.pdf

[11] J. Rosado and S. Hidalgo, "Characterization and modeling of crosstalk and afterpulsing in Hamamatsu silicon photomultipliers", Journal of Instrumentation, **10**, P10031 (2015)

[12] W. R. Leo, "Techniques for Nuclear and Particle Physics Experiments", Springer-Verlag (1987)

[13] J. Fleury, S. Callier, C. de La Taille, N. Seguin, D. Thienpont, F. Dulucq, S. Ahmada and G. Martin, "Petiroc and Citiroc: front-end ASICs for SiPM read-out and ToF applications", Journal of Instrumentation, **9**, C01049 (2014)

[14] S. Callier, C. De La Taille, G. Martin-Chassard, L. Raux, "EASIROC, an easy & versatile ReadOut device for SiPM" (2011), https://indico.cern.ch/event/102998/contributions/17281/attachments/10609/15510/SC_Easiroc_TIPP11.pdf

[15] D. Impiombato, S. Giarrusso, M. Belluso, S. Billotta, G. Bonanno, O. Catalano, A. Grillo, G. La Rosa, D. Marano, T. Mineo, F. Russo, G. Sottile, "Characterization of the front-end EASIROC readout of SiPM in the ASTRI camera" Nuclear Physics B (Proceedings Supplements), 239, 254 – 257 (2013)

[16] D. Impiombato, S. Giarrusso, T. Mineo, M. Belluso, S. Billotta, G. Bonanno, O. Catalano, A. Grillo, G. La Rosa, D. Marano, G. Sottile, "Characterization of the EASIROC as front-end for the readout of the SiPM at the focal plane of the Cherenkov telescope ASTRI", Nucl. Instr. And Meth. A, 729, 484 – 490 (2013)

[17] D. Marano, G. Bonanno, S. Billotta, M. Belluso, A. Grillo, S. Garozzo, G. Romeo, O. Catalano, G. La Rosa, G. Sottile & D. Impiombato, "PSPICE High-Level Model and Simulations of the EASIROC Analog Front-End", International Journal of Modelling and Simulations, 34, 175 – 186 (2015)

[18] D. Impiombato, S. Giarrusso, T. Mineo, G. Agnetta, B. Biondo, O. Catalano, C. Gargano, G. La Rosa, F. Russo, G. Sottile, M. Belluso, S. Billotta, G. Bonanno, S. Garozzo, D. Marano, G.; Romeo, "Evaluation of the optical cross talk level in the SiPM adopted in ASTRI SST-2M Cherenkov using EASIROC front-end electronics", Journal of Instrumentation, 9, article id. C02015 (2014)

[19] D. Impiombato, S. Giarrusso, T. Mineo, O. Catalano, C. Gargano, G. La Rosa, F. Russo, G. Sottile, S. Billotta, G. Bonanno, S. Garozzo, A. Grillo, D. Marano, G. Romeo,

“Characterization and performance of the ASIC (CITIROC) front-end of the ASTRI camera”, Nucl. Instr. And Meth. A, 794, 185 (2015).

Nuclear Inst. and Methods in Physics Research, A 885 (2018) 7–14

Contents lists available at ScienceDirect

Nuclear Inst. and Methods in Physics Research, A

journal homepage: www.elsevier.com/locate/nima

Correlation methods for the analysis of X-ray polarimetric signals

E. Massaro [a,b], S. Fabiani [a,*], R. Campana [c], E. Costa [a], E. Del Monte [a], F. Muleri [a], P. Soffitta [a]

[a] IAPS-INAF, Roma, Italy
[b] In Unam Sapientiam, Roma, Italy
[c] IASF-INAF, Bologna, Italy

ARTICLE INFO

Keywords:
X-ray polarimetry
Stokes' parameters
Polarimetry detectors
Polarimetric data analysis
Photoelectric polarimeters
Compton polarimeters

ABSTRACT

X-ray polarimetric measurements are based on studying the distribution of the directions of scattered photons or photoelectrons and on the search of a sinusoidal modulation with a period of π. We developed two tools for investigating these angular distributions based on the correlations between counts in phase bins separated by fixed phase distances. In one case we use the correlation between data separated by half of the bin number (one period) which is expected to give a linear pattern. In the other case, the scatter plot obtained by shifting by 1/8 of the bin number (1/4 of period) transforms the sinusoid in a circular pattern whose radius is equal to the amplitude of the modulation. For unpolarized radiation these plots are reduced to a random point distribution centred at the mean count level. This new methods provide direct visual and simple statistical tools for evaluating the quality of polarization measurements and for estimating the polarization parameters. Furthermore they are useful for investigating distortions due to systematic effects.

1. Introduction

Measurements of the linear polarization in the X-ray band are based on the detection of anisotropies either in the angular distribution of scattered photons or in the initial direction of photoelectrons (for a comprehensive review see the book by Fabiani and Muleri [1]). The latter technique appears now more promising with the development of the Gas Pixel Detector (hereafter GPD) [2–4] that will be the focal plane instrument of the first polarimetric mission after the pioneering age of OSO 8. Indeed IXPE (Imaging X-ray Polarimetry Explorer, Weisskopf et al. [5]) has been selected as the next SMEX NASA mission for a flight in late 2020. With three mirrors and three GPDs it will perform spectral–temporal–angular resolved polarimetry as a break-through measurement in astrophysics, allowing the opening of a new window on the high-energy sky. Meanwhile XIPE (X-ray Imaging Polarimetry Explorer) [6], has completed its phase A study in the framework of the 4th ESA call for a medium size mission.

In the present paper we show some simple correlation methods useful for the detection and for the parameter estimates of a polarized signal. These methods are based on the phase distribution histograms of photons (or electrons) and do not require measurements of the Stokes' parameters; for this reason they have the advantage of simplifying the statistical tools used for evaluating the significance of the polarimetric estimates [7]. Our new method is therefore complementary to the classical Stokes' analysis.

This topic has been previously studied by different authors. The relation between sensitivity and significance of a polarization measurement [8,9] has been revisited by means of simulation [10]. The use of Stokes' parameters for X-ray polarimetry has been explored by Kislat et al. [11] while the possibility to extend the standard tools of X-ray astronomy (XSPEC) to polarization by using Stokes parameter has been studied very recently by Strohmayer [12]. Other authors, instead, investigated the possibility of using Bayesian methods to derive the polarization angle and degree, which may be interesting when low signal-to-noise ratio are expected [13,14].

An important issue in polarization measurements is the possibility to have a noise distribution differing from the Poissonian one because of intrinsic effects in the detection technique. For instance, in a photoelectric polarimeter as the GPD the uncertainty on the initial direction of the photoelectron can be influenced by the hexagonal geometrical pattern of pixel plane (especially for tracks comprising a very small number of pixels) producing a not uniform spread of angular directions in the phase histograms [15].

Thus the assumption that the noise on the angular distribution is white and purely Poissonian cannot be always verified. Our correlation methods are not based on this assumption and provide direct visual

* Corresponding author.
E-mail address: sergio.fabiani@iaps.inaf.it (S. Fabiani).

https://doi.org/10.1016/j.nima.2017.12.056
Received 26 May 2017; Received in revised form 15 December 2017; Accepted 19 December 2017
Available online 23 December 2017
0168-9002/

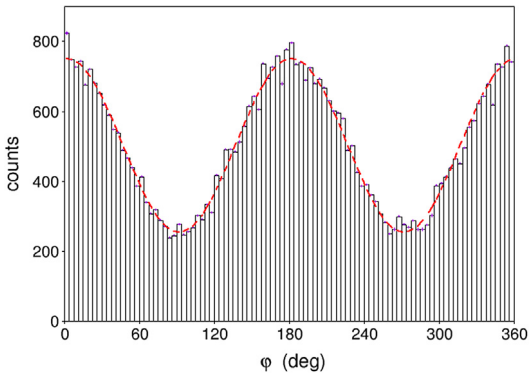

Fig. 1. Histogram of the angular distribution of the initial direction of electrons due to a polarized X-ray flux. The dashed curve is the best fit modulation.

tools for evaluating the quality of polarization measurements and for investigating distortions due to systematic effects.

2. Polarization data

For each detected photon the information on its linear polarization is given by the azimuthal angle φ measured from the direction of a scattered photon (for scattering polarimeters) or from the initial direction of the photoelectron trajectory (for photoelectric polarimeters). The detection of a polarization is therefore obtained from the angular distribution of the φ values of a number N of observed photons and particularly from the amplitude of a sinusoidal modulation with a period of π (or 180°), due to the differential cross section of the physical process involved (Compton scattering and photoelectric absorption, respectively). In the following we will refer to this histogram as the data set $\{n_k | k = 1, \dots, M\}$, with a total bin number M and a number of events in the kth bin indicated by n_k. One can write the expected modulation curve as

$$n(\varphi_k) = A \ \sin(2(\varphi_k + \psi)) + \langle n \rangle \quad , \tag{1}$$

where $\varphi_k = (2\pi/M)(k - 1/2)$ is the phase of the bin centre, A the amplitude of the modulation and ψ is the polarization angle; for a total number of photons N one obviously has

$$\langle n \rangle = N/M \quad . \tag{2}$$

In Fig. 1 the histogram of a modulation curve of experimental data for a totally polarized source is shown. The polarization degree p of the incoming signal is then evaluated by

$$p = \frac{1}{\mu} \frac{A}{\langle n \rangle} \quad , \tag{3}$$

where μ is the instrumental modulation factor, i.e. the amplitude resulting from a totally polarized input radiation. The noise is due to the statistical fluctuations of counts and to possible instrumental effects.

As it will be clear in the following it is advantageous to consider M as a multiple of 8 (in the following examples we will consider bin numbers with this property).

3. The method of the linear correlation plot

We create a scatter plot with $M/2$ points having coordinates $(n_k, n_{k+M/2})$ $(1 \le k \le M/2)$. If a polarization modulated signal is present, these point will be distributed along a straight segment with an inclination of 45° and with a length equal to the double of the modulation amplitude. The linear correlation coefficient r can provide useful information for estimating the statistical S/N ratio. The significance of the polarization measurement is obtained from the likelihood to have a corresponding r with $M/2$ degrees of freedom. The linear plot for the same data set in Fig. 1 is given in Fig. 2 (left panel), where the values of the linear correlation coefficient and of the best fit line parameters are also reported together with the statistical uncertainties:

$$n_{k+M/2} = h + s \ n_k \tag{4}$$

are also reported.

For a modulation as the one of Eq. (1) the expected values of the slope s is 1 and of the constant h is zero and it is actually found within 1 standard deviation as shown in Fig. 2 (left panel). In the case of a non polarized radiation we expect no correlation between the phase bins and in the plot the corresponding points will be randomly distributed around the mean value, with a linear correlation coefficient close to zero.

It is well known from the correlation theory that r^2 is the fraction of the variance *explained* by the linear regression and that $1 - r^2$ is proportional to the *residual* variance due to the noise; thus the simplest way to evaluate the S/N ratio of the polarization is given by $\sqrt{r^2/(1 - r^2)}$. We stress that this simple formula is independent of any assumption of the nature of the noise and particularly if it is only due to the Poisson statistics or to the occurrence of possible systematic effects. In particular values of s and/or h non consistent with 1 and zero, respectively, likely indicate a systematic deviation.

A linear correlation with unit slope results not only from a sinusoidal pattern like that of Eq. (1), but also from any distribution with a period $M/2$, and thus this plot is not useful for detecting a polarized signal itself, but only for estimating the S/N ratio and the occurrence of some systematic effects. These in fact can introduce changes in the amplitude of the angular distribution resulting in a value of the slope s different from unity. For instance, systematic deviations affecting an odd harmonic, like the 3rd one, which are anticorrelated and therefore the expected value is $s = -1$, would produce a decrease of the slope (see Section 7).

4. The method of the circular plot

A useful tool for measuring the polarization parameters and for a quick inspection of data is based on the scatter plot of the histogram of the angular distribution of events in the (ξ, η) space, where these quantities are the histogram bin counts with the latter one shifted by $M/8$ bins. Consider the distribution of M points having the coordinates $(\xi_k = n_k, \eta_k = n_{k+M/8})$, $(1 \le k \le 7M/8)$, completed with the $M/8$ points $(\xi_k = n_k, \eta_k = n_{k-7M/8})$, $(7M/8 + 1 \le k \le M)$. If the counts are distributed with a $\sin(2\varphi)$ modulation the phase difference of $M/8$ corresponds to 1/4 of the period and the points in the (ξ, η) space will be distributed in a circular pattern having the radius equal to the modulation amplitude. Thus the problem of detecting a polarization is then reduced to that of finding such a circular distribution of data.

4.1. Measure of the polarization degree and angle

For each point of the plot we can compute the corresponding radius R_k

$$R_k = \sqrt{(n_k - \langle n \rangle)^2 + (n_{k+M/8} - \langle n \rangle)^2} = \sqrt{(\xi_k - N/M)^2 + (\eta_k - N/M)^2} \tag{5}$$

The distribution of R_k against the phase bin number angle or the bin centre angle φ_k is expected to be consistent with a constant and the ratio between the mean value of the radius $\langle R \rangle$ and its standard deviation σ_R is an estimator of the S/N ratio. In Fig. 2 (right panel) it is reported the circular polarization plot for the same data set of the left panel. The mean radius is $\langle R \rangle = (249.20 \pm 2.8)$. The amplitude found by the usual method of a $\sin(2(\varphi - \psi))$ least-squares fitting results $A = (247.5 \pm 3.6)$, compatible with the previous estimate within 1σ.

Note that in the circular plot each value n_k is used two times: first for computing η and then for ξ; thus the M values distributed in the two

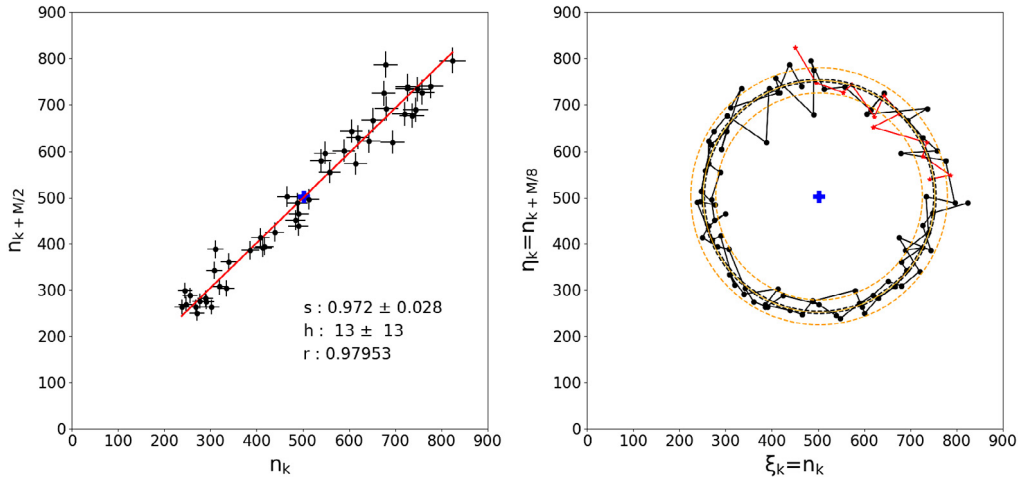

Fig. 2. Left panel: scatter plot exhibiting the linear correlation between the first and second sections of a 96 bin angular distribution in Fig. 1. Errors are evaluated assuming a Poisson distribution of counts in the histogram bins. The solid line is the linear best fit whose slope s and intercept h are given in the bottom of the figure with the correlation coefficient r. The fit is performed with the orthogonal distance regression method implemented in the python package *scipy.odr* based on the ODRPACK FORTRAN-77 library (https://docs.scipy.org/doc/external/odrpack_guide.pdf). The point representing the means of two sections' values is the bold cross. Right panel: scatter plot of the same data exhibiting the circular pattern due to the shift of $M/8$ data shift in a 96 bin angular distribution. Star points connected by the red line are those of the circular completion. The solid line circle has a radius equal to the average radial distance from the centre marked by the cross. The blue dashed lines closer to solid line circle show the uncertainty on the average radius, while the larger orange dashed lines represent the standard deviation of the distribution of radii. (For interpretation of the references to colour in this figure legend, the reader is referred to the web version of this article.)

circles are not independent. For instance, a large positive fluctuation in one of the $\{n\}$ values would correspond to two values of R_k in excess, the former one in the η component and, after $M/8$ points, in the ξ component. According to Eq. (3), the polarization degree p is given by

$$p = \langle R\rangle/(\mu\ \langle n\rangle) = \frac{\sum_k R_k}{\mu N} \quad . \tag{6}$$

Since the peaks of the modulation curve correspond to the maximum value of the n_k coordinate with respect to the centre of the circular correlation plot, the information on the polarization angle ψ is also in the circular distribution. The polarization angle corresponds to the angle of the initial point of the data set with respect to the positive direction of the $\xi_k = n_k$ axis. By rotating the polarization angle the starting point of the circular correlation plot rotates. This is shown in left panel of Fig. 3 where the same data of Fig. 2 are plotted (black dots) together with the points obtained by a negative phase shifting of 60° of the same histogram (red points). We can thus correlate the angles γ_k of segments from the centre of the circle to each point and ξ axis with the angles φ_k giving the central phase of the bin moving progressively along the histogram. The former angles can be computed from

$$\sin\ \gamma_k = (\eta_k - N/M)/R_k \quad , \quad \cos\ \gamma_k = (\xi_k - N/M)/R_k \tag{7}$$

and the relation between these two angles must be the straight line

$$\tilde{\gamma}_k = -2\varphi_k + \psi = -2(k-1/2)(360^\circ/M) + \psi \tag{8}$$

where the factor 2 takes into account the second harmonic modulation. We remark that the angle quadrant must be properly assigned to take into account the two clockwise rounds described by the radius for increasing k. For this reason the expected linear relation between γ_k and φ_k has the slope equal to −2. The negative sign is due to the anticlockwise direction of data in the circular plot; it can be inverted in computation without loss of information.

The resulting linear relations are shown in the right panel of Fig. 3 for the original and shifted data sets. The slope is very close to the expected value and also the intercepts agree well with 0° (for the original data) and −60° (for the shifted data) within the histogram bin width of 3°.75.

This calculation must be performed over M values, corresponding to two complete rounds in the circle with increasing angles and consequently, for the bins in second half of the histogram, a constant equal to 360° must be added when necessary to data and thus the two complete rounds correspond to 720°. If $\langle\gamma\rangle$ would be computed over a single round ($M/2$ values) the constant 360° must be decreased to 180°. It is easy to verify that, considering the slope fixed at −2, the best estimate of ψ is simply

$$\psi = 360^\circ + \langle\gamma\rangle \tag{9}$$

as expected from a vertical shift of the data.

4.2. Variance of the parameters of a circular plot

It is interesting to study how the variance of the radius R is related to the variance of the set $\{n\}$.

$$R_k^2 = (n_k - \langle n\rangle)^2 + (n_{k+M/8} - \langle n\rangle)^2 \tag{10}$$

and

$$\langle R^2\rangle = \frac{1}{M}\sum_{k=1}^{M}\left[(n_k - \langle n\rangle)^2 + (n_{k+M/8} - \langle n\rangle)^2\right] = 2\sigma_n^2 \tag{11}$$

that for unpolarized data is equal the Poissonian variance N/M. One has also

$$\Delta R_k = \sqrt{(n_k - \langle n\rangle)^2 + (n_{k+M/8} - \langle n\rangle)^2} - \langle R\rangle \tag{12}$$

and

$$\begin{aligned}\sigma_R^2 &= \langle(\Delta R)^2\rangle = \frac{1}{M}\sum_{k=1}^{M}[R_k^2 + \langle R\rangle^2 - 2\langle R\rangle R_k] \\ &= \langle R^2\rangle - \langle R\rangle^2 = 2\sigma_n^2 - \langle R\rangle^2\end{aligned} \tag{13}$$

then

$$\sigma_R^2 = 2(\sigma_n^2 - \frac{1}{2}\langle R\rangle^2) \quad . \tag{14}$$

The standard deviation of the mean $\langle R\rangle$ then will be

$$\sigma_{\langle R\rangle} = \frac{1}{\sqrt{M}}\ \sigma_R = \frac{1}{\sqrt{M}}\sqrt{2\sigma_n^2 - \langle R\rangle^2} \quad . \tag{15}$$

For the polarization degree we have:

$$\sigma_p = \sigma_{\langle R\rangle}/[\mu(N/M)] = \frac{\sqrt{M}}{\mu N}\sqrt{2\sigma_n^2 - \langle R\rangle^2} \quad . \tag{16}$$

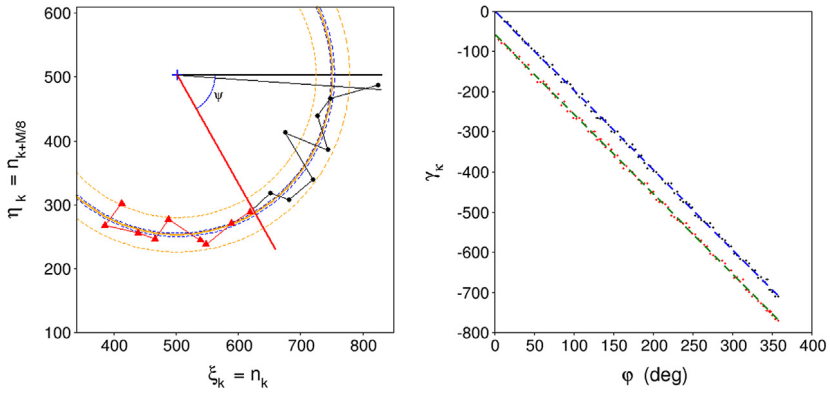

Fig. 3. Left panel: the initial part of the annular distribution of the original data and with a negative phase shift of 60°. The starting point of the circular distribution is sensitive to the phase shift and therefore to the polarization direction. Right panel: the linear relation between the angles γ_k, estimated from the circular plot in the lower panel of Fig. 2, and the expected values from the bin phases φ_k. Original data are the filled circles points and the dashed line is the best fit. The lower data set (filled squared points) and their best fit (solid line) are obtained from the same histogram applying a backward shift of 8 bins (equal to 30°). The slope best fit value is -1.988 ± 0.005 and the intercept values are $2°.01 \pm 1°.14$ and $-57°.3 \pm 1°.15$.

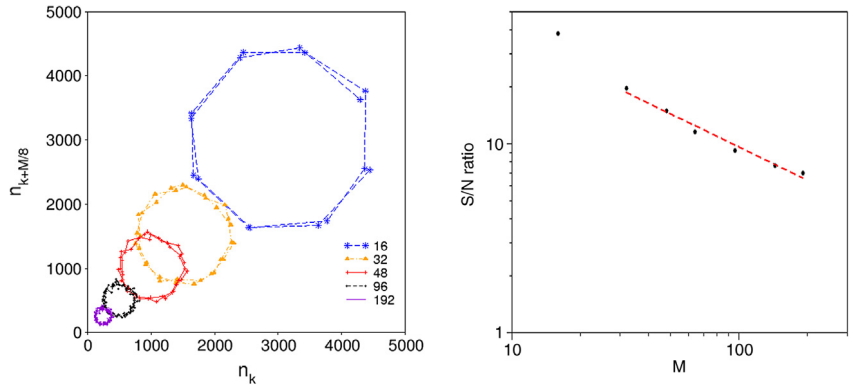

Fig. 4. Left panel: circular plots of the experimental data of Fig. 1 with a different number of bins ranging from 16 to 192. Right panel: the S/N of the same data set of the left panel for different number of bins M. The best fit with a power law from 32 to 192 bins is represented by the dashed red line.

From Eq. (9) we see that the standard deviation of the polarization angle σ_ψ is the same of $\langle\gamma\rangle$, which can be computed by standard error propagation taking into account the right covariance term $\langle\gamma R\rangle - \langle\gamma\rangle\langle R\rangle$ because these values are used in the calculation of the sine or cosine functions in Eq. (7).

4.3. The histogram bin number and the S/N ratio

The S/N ratio of the polarization measure is given by $\langle R\rangle/\sigma_R$ that measures how large is the distance of the mean circle from the its centre in units of the standard deviation of R. The use of $\sigma_{\langle R\rangle}$ instead of σ_R is not correct because it does not take into account the actual dispersion of R values around its mean and will give a higher S/N value.

The S/N ratio is highly affected by the choice of the histogram number of bins M. A high M, in fact, reduces the number of events in each bin and the statistical fluctuations on n_k are approximately proportional to $\sqrt{M}$. This is equivalent to a finer sampling and therefore to add higher frequency components in the Fourier spectrum: practically, the dispersion of the radius values increases, but the relative error on the mean value $\langle R\rangle$ remain stable because it is divided by $\sqrt{M}$. Conversely, the effect of a low bin number is equivalent to apply a smoothing to the histogram, filtering the all the high frequency noise, with a consequent increase of the S/N ratio.

To illustrate this effect we performed a test with some selected values of M, ranging from 16 to 192, on the experimental data set in Fig. 1. The resulting circular plots are shown in the left panel of Fig. 4. The S/N ratio evaluated by means of the previous formula changes from 38.3 and 20 for 16 and 32 bins, respectively to 7.0 for 192 bins, while the relative error of the mean radius remains constant around 1% as well as the accuracy of the estimates of the polarization degree and angle. The S/N of the same data set is shown in the right panel Fig. 4. The best fit with a power law from 32 to 192 bins gives an exponent equal to −0.58, in a reasonable agreement with the expected −0.5. Note that in the left panel of Fig. 4 the circle for $M = 16$ is reduced to an octagon because there are only 8 points for each round. This is reasonably the lowest bin number to be used for detecting polarization, although the use of 24 bins appears a right trade-off between an optimal S/N ratio and well defined circular plot. For some instruments, as in the case of scattering polarimeters, the maximum bin number is fixed by the number of detectors and the use of 24 or 16 bins could not be admissible. This problem should be considered in the design of the instrument.

5. Numerical simulations

We used numerical simulations of polarization angular distributions, assuming that fluctuation are due to a Poissonian statistics, for investigating some statistical properties of the proposed tools. Fig. 5 reports the same plots of Fig. 2 but for simulated data for an unpolarized (black points) and 40% polarized signals with histograms of 192 angular bins for a total number of 5×10^5 events. Points of the former do not track any line (upper panel) or circle (lower panel) and appear randomly distributed around the mean value of counts.

The capability of our tools for measuring the polarization is also shown by the linear correlation plot in the upper panel of Fig. 5: here the unpolarized data have a correlation coefficient has the low value $r = -0.1987$, while in the case of the polarized data it results $r = 0.9938$,

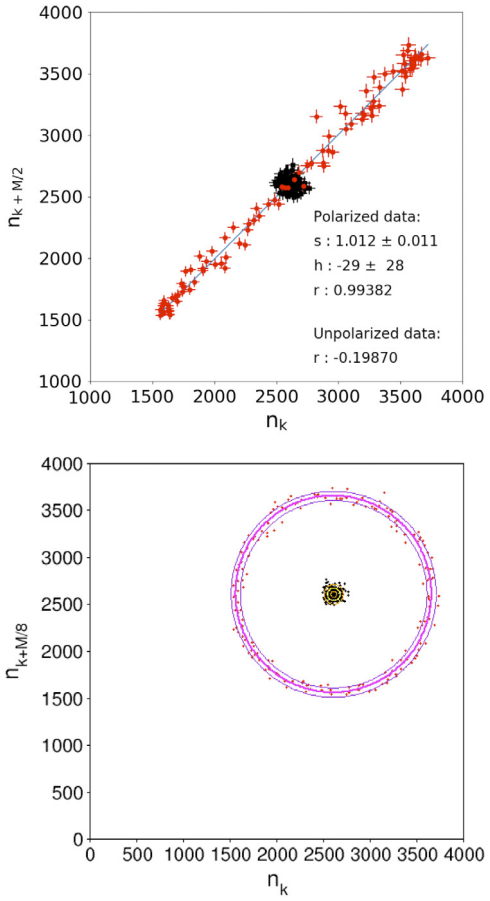

Fig. 5. Scatter plots of the linear (upper panel) and circular (lower panel) correlation for the same simulated data collected in 192 bin of the angular distribution. The filled squared points represent an unpolarized signal, while the filled circle points represent a signal 40% polarized. The solid line in the upper panel is the best fit of the polarized data. The solid and dashed circles in the lower panel have radii equal to the average and $\pm 1\sigma$ outer and inner circles, respectively.

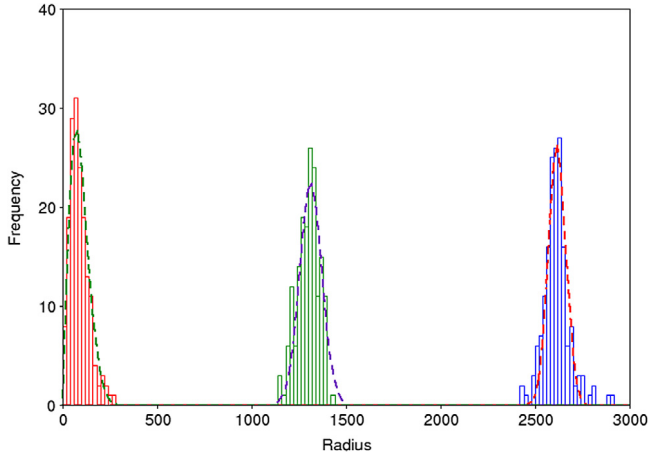

Fig. 6. Histograms of the radial values for the three simulated data with different polarizations. The histogram of the unpolarized signal (on the left side) appears well described by a Rayleigh function given by the Eq. (17) (dashed line). The polarized signals at 50% (histogram in the centre) and 100% (histogram on the right side) are described by the Plaszczynski et al. function as expressed in Eq. (19) (fitted dashed lines).

and therefore only the ≈1.2% of the total variance is due to statistical noise. Note that in the circular plot the mean value of the radial distance between data points and the centroid is always different from zero; in Fig. 5 it defines the solid circle, that in this case is 67.3, but this value is lower than 2 standard deviation (outer and inner solid circles corresponding to 1σ), indicating that the resulting polarization degree is not statistically significant.

In the case of 40% polarized histogram the mean radius of the circular distribution is $\langle R\rangle = 1046.45$ with a standard deviation of $\sigma_R = 48.72$. Therefore the S/N is more than 21 standard deviations. The estimated value of the polarization degree is 0.4010 ± 0.0013 (see Eqs. (6) and (16)), in a fully agreement with the simulation input parameter and coincident with the sinusoidal best fit, as expected.

5.1. Distribution functions of R_k

It is possible to perform numerical simulations to obtain the histograms of the radial distances R_k: in Fig. 6 we present three cases obtained from 192 bin histograms of an unpolarized signal, a 50% polarized signal and a 100% polarized signal. As apparent in Fig. 5 the data points are distributed with a random orientation with respect to the centroid of their coordinates, given by the mean value of the counts; therefore their radial distances follows the well known Rayleigh distribution:

$$f(R) = \frac{R}{\sigma^2}\, e^{-R^2/2\sigma^2} \quad , \tag{17}$$

This formula is normalized to the unity and its mean value and variance are equal to $\sigma\sqrt{\pi/2}$ and $(2-\pi/2)\sigma^2$, respectively.

For a polarized signal the points spread around the centre located in the ξ,η plane at the position $[\langle n\rangle, \langle n\rangle]$; their distance to this centre changes because the fluctuations of counts in the phase histogram following a Poisson's statistics that is very well approximated by a Gaussian law. We stress that in principle the *thickness* of the point annulus is not uniform because the Poissonian fluctuations are given by the square root of n_k and therefore their amplitude changes with the bin counts: we expect then a thickness larger in the upper-right sector and narrower in the lower-left sector. This effect can be easily estimated considering that the highest and lowest counts for a polarized signal with a resulting fractional modulation amplitude $a = A/\langle n\rangle$ are given by $\langle n\rangle(1+a)$ and $\langle n\rangle(1-a)$, respectively; thus the difference of their standard deviations are

$$\Delta\sigma = \sqrt{\langle n\rangle}(\sqrt{1+a} - \sqrt{1-a}) \approx a\sqrt{\langle n\rangle} \quad , \tag{18}$$

thus, for typical modulation amplitudes $a < 0.3$ the change in the thickness of the annulus with respect to the mean can be considered rather small. Assuming that the annulus thickness is nearly constant, we approximated the distribution of radius values with the slightly asymmetric law given Plaszczynski et al. [16]:

$$f(R) \approx \sqrt{\frac{R}{2\pi\langle R\rangle}}\,\frac{1}{\sigma}\,\exp\{-(R-\langle R\rangle)^2/2\sigma^2\} \quad . \tag{19}$$

In Fig. 6 is shown the radial distributions of the data resulting from simulations. The histogram of an unpolarized signal (on the left side) appears well described by a Rayleigh function given by the Eq. (17) (dashed line). The polarized signals at 50% (histogram in the centre) and 100% (histogram on the right side) are described by the Plaszczynski et al. function as expressed in Eq. (19) (dashed lines). As a simple criterion Eq. (17) should be preferred to Eq. (19) when $\sigma \approx \langle R\rangle$. From these approximations one can compute the moments of the distributions useful for statistical investigations.

6. The Stokes' parameters

The most usual method to estimate the polarization parameters is to compute the Stokes' parameters, that in the case of a linear polarization measured by means of an angular histogram of counts are (see, for instance, Kislat et al. [11]):

$$Q = \sum_{k=1}^{M} n_k\, \cos(2\varphi_k) \;,\; U = \sum_{k=1}^{M} n_k\, \sin(2\varphi_k) \;,\; I = \sum_{k=1}^{M} n_k \tag{20}$$

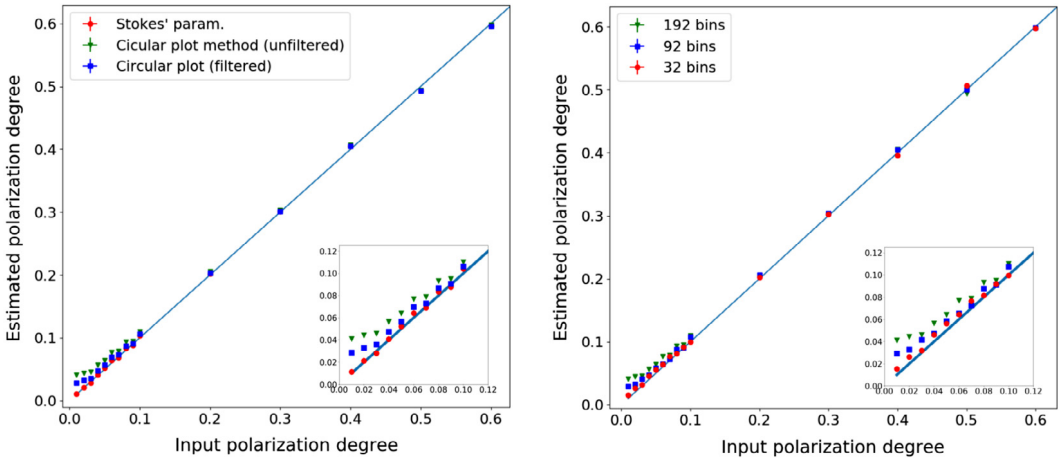

Fig. 7. Left panel: comparison between polarization estimated obtained by means of the Stokes' parameters (filled circles) vs the circular plot method (unfiltered: downward triangles, filtered: filled squared points). Right panel: the comparison between polarization estimated obtained by applying the unfiltered circular correlation method with a different binning of the modulation histograms. The green downward triangles in two panels refer to the same data (unfiltered circular correlation method) applied to a modulation histogram with 192 bins.

from which one obtains

$$p = \frac{2}{\mu}\frac{\sqrt{Q^2+U^2}}{I} \quad , \quad \psi = \frac{1}{2}\arctan(U/Q) \quad . \tag{21}$$

Of course, when applied to the previously considered data sets the results turns out fully consistent with other estimates: for instance, in the case of the simulated data of Fig. 5, we found again $p = 0.401$, indicating that our circular plot method that is bias free.

It is clear from the scalar products of the first two formulae of Eq. (20) that they are the second harmonic cosine and sine components of the Fourier series. It is therefore very important to properly take into account the amplitude distribution over all the other frequencies due to noise fluctuations to evaluate the correct significance of the measure. The estimate of the statistical uncertainties of the polarization parameters requires an accurate treatment as demonstrated in the paper by Kislat et al. [11].

To compare the performances of these two methods we produced a set of simulated histograms with polarization degrees varying from 100% down to 1% with an instrument modulation factor $\mu = 0.5$ and a total number of events $N = 10^6$ distributed in 192 phase bins. A Poissonian noise was added to the counts in each bins with a variance equal to n_k.

In our method (circular plot) the statistical properties of data are entirely preserved. This is clearly illustrated by the plot in the left panel of Fig. 7, where the results of the application of the two methods to simulated histograms are presented: the estimated p values are coincident down to about 10%; for lower values the polarization degree obtained by the Stokes' parameters (filled circles) remain very close to the expected ones, while those from the circular plot (downward triangles) are systematically higher approaching to a constant value of ∼4%. For low polarization degrees the R values practically follow a Rayleigh distribution whose mean value is highly depending on the p/σ_p ratio. After applying a noise reduction by means of simple running average smoothing over three consecutive histogram bins the resulting p turns out to be closer to the expected values (filled squared points). A stronger smoothing would further improve the estimates.

As discussed in Section 4.3, the choice of a low bin number in the histogram is equivalent to a filtering. We expect therefore that the results of the circular plots are more and more similar to those obtained by means of the Stokes' parameters when reducing the number of bins. To verify this point we used the same simulation tool to produce histograms with M ranging from 32 to 192 and evaluated the polarization degree. The results are plotted in the right panel of Fig. 7 where green downward triangles in both panels refer to the same data set (unfiltered circular correlation method) applied to a modulation histogram with 192 bins. It is clearly apparent that the use of the lowest M value makes possible to detect polarizations as low as those obtained by means of the Stokes' parameters.

This comparison shows also that the calculations of the Stokes' parameters based only on the amplitude of the second harmonic must be considered as a "self-filtered" method and therefore it does not take entirely into account the noise which affects all the other harmonics. Thus, to evaluate the significance of the results one has to study the statistical properties of the histogram. The use of the unfiltered circular plot contains all the information on the noise, including systematic deviations if present, and thus it provides a direct evaluation of the sensitivity reached in the measurements.

7. Systematic effects and the correlation method

The occurrence of systematics effects can affect the measurement and the use of correlation plots can help in their detection. In scattering polarimeters, for example, a geometrical misalignment or a different efficiency of event detection in some angular channels can modify the azimuthal modulation of events in such a way that Eq. (1) does not describe properly any more the angular distribution of the signal modulation.

We describe how a simple systematic effect modifies the correlation plots. Let us assume a lowering of the gain that produces a decrease of detected counts for angular directions higher than a certain value. Then Eq. (1) is modified as follows by step function:

$$n(\varphi_k) = n(\varphi_k) \cdot g(\varphi_k) \tag{22}$$

where

$$g(\varphi_k) = \begin{cases} 1, & \text{if } \varphi_k \le 210^\circ \\ \varepsilon, & \text{if } \varphi_k > 210^\circ \end{cases} \tag{23}$$

We consider here the case of a high gain difference ($\varepsilon = 0.8$) to make more evident how the correlation plots are modified. The effects on the linear (left panel) and circular (right panel) correlation distribution are reported in Fig. 8 which must be compared with those in Fig. 2. In the linear correlation plot three changes are apparent: (i) the expected mean value of counts per bin (N/M) is now different from the mean value in the first ans second half of the phase histogram and therefore it is far from the regression line; (ii) the dispersion of data points with respect to the best fit is highly not uniform, being the points in the upper section much more scattered than in the lower one; (iii) the regression parameters are different from the expected ones, in particular the slope is reduced to (0.931 ± 0.040) and the intercept h is (-0.43 ± 19) and it differs from the expected value by about 2 standard deviations.

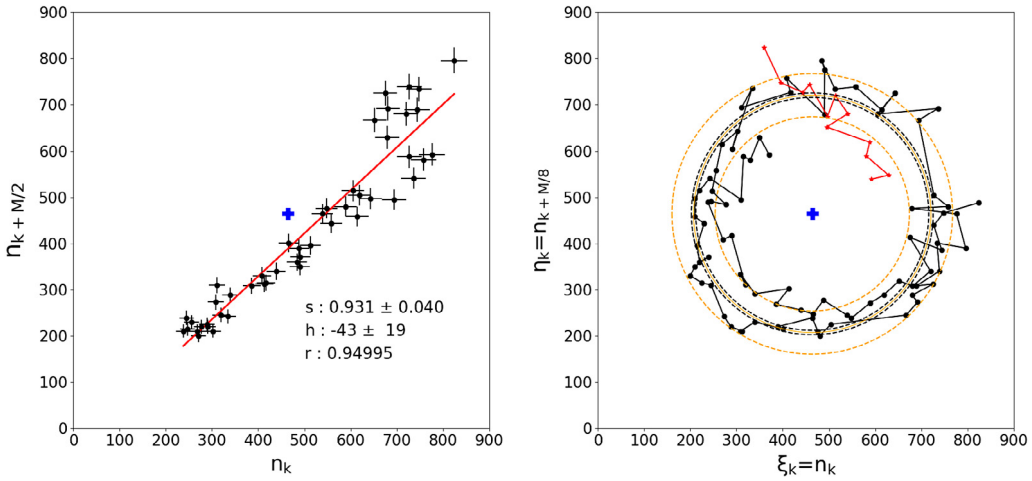

Fig. 8. Left panel: the linear correlation plots by assuming an event detection efficiency for angles larger than 210° decreased by 20%. The best fit values of the linear regression (orange line) and the correlation coefficient are reported. Right panel: the circular correlation plot in the same case. Note the splitting of the rings in two separated tracks.

The circular plot of the same data shows a well clear separation of two branches, particularly apparent in the low count rate sector where the outer branch is due to the lower count statistics on the bins after the fixed angular direction. The same effect is present in the circular completion of the plot (red points). We see, therefore, that even a simple inspection of these correlation plots can be useful for highlighting possible deviations from the expected behaviour.

8. Conclusion

We proposed two simple tools for measuring the polarization parameters based on correlations between pairs of bins in the angular distribution having assigned shifts.

We studied by means of laboratory data and numerical simulations how the results of the circular plot method depend upon the histogram binning. In particular, we showed that in the correlation method the noise components at high frequencies is reduced by using a low number of bins in the modulation histogram as well as by applying a smoothing. No particular assumptions were made on the origin of the noise (for instance, if it is due entirely to Poissonian fluctuations or if there are other systematic contributions) for computing the S/N ratio and variance of the estimated parameters' values. The estimate of the polarization degree and its significance is independent of the angle, that follows by a simple linear fit. The results were found fully consistent with those obtained by other methods, as the evaluation of Stokes' parameters. Moreover, the correlation plots are direct and efficient visual tools for fast detection of a polarized signal and the occurrence of systematic deviations.

Finally, the statistical properties of the circular distribution can be derived in a straightforward way: for instance, for an unpolarized signal the radial distribution of points in the circular plot follows the Rayleigh distribution because their distances from the centre are those expected by a random Gaussian process, while the one proposed by Plaszczynski et al. [16] appears rather well appropriate distribution when there is a clear annular pattern due to the presence of a significant polarization degree.

This method can be eventually included in the quick look data analysis of scientific data of XIPE [6]. Moreover, these tools are well suited for the analysis of data obtained by scattering polarimeters where the absorber is segmented into several scintillator elements (see, for instance, the COMPASS project by Del Monte et al. [17]) and the angular distribution is directly obtained as an histogram.

Acknowledgements

We are grateful to the referee K. Jahoda for his careful revision and **germinating** comments, that contribute to make clearer our text. This work was performed as an activity for the development of the XIPE (X-ray Imaging Polarimetry Explorer), IXPE (Imaging X-ray Polarimetry Explorer) and COMPASS (COMpton Polarimeter with Avalanche Silicon readout) projects. XIPE is one of the three mission candidates to the M4 launch opportunity of the European Space Agency (ESA). The Italian participation to the XIPE study is funded by the Agreement ASI-INAF n. 2015-034-R.0. IXPE is an Explorer mission approved by NASA. Italian contribution to IXPE mission is supported by the Italian Space Agency through agreement ASI-INAF n. 2017-12-H.0 and ASI-INFN agreement n. 2017-13-H.0. COMPASS is funded under grant TECNO INAF 2014.

References

[1] S. Fabiani, F. Muleri, Astronomical X-Ray Polarimetry, Aracne Editrice, Oct. 2014.
[2] E. Costa, P. Soffitta, R. Bellazzini, A. Brez, N. Lumb, G. Spandre, An efficient photoelectric X-ray polarimeter for the study of black holes and neutron stars, Nature 411 (2001) 662.
[3] R. Bellazzini, G. Spandre, M. Minuti, L. Baldini, A. Brez, F. Cavalca, L. Latronico, N. Omodei, M.M. Massai, C. Sgro', E. Costa, P. Soffitta, F. Krummenacher, R. de Oliveira, Direct reading of charge multipliers with a self-triggering CMOS analog chip with 105 k pixels at 50 μm pitch, Nucl. Instrum. Methods Phys. Res. A 566 (2006) 552.
[4] R. Bellazzini, G. Spandre, M. Minuti, L. Baldini, A. Brez, L. Latronico, N. Omodei, M. Razzano, M.M. Massai, M. Pesce-Rollins, C. Sgró,, E. Costa, P. Soffitta, H. Sipila, E. Lempinen, A sealed gas pixel detector for x-ray astronomy, Nucl. Instrum. Methods Phys. Res. A 579 (2007) 853.
[5] M.C. Weisskopf, B. Ramsey, S. O'Dell, A. Tennant, R. Elsner, P. Soffitta, R. Bellazzini, E. Costa, J. Kolodziejczak, V. Kaspi, F. Muleri, H. Marshall, G. Matt, R. Romani, The Imaging X-ray Polarimetry Explorer (IXPE), in: Proc. SPIE, Vol. 9905, in: Society of Photo-Optical Instrumentation Engineers (SPIE) Conference Series, 2016, p. 990517.
[6] P. Soffitta, R. Bellazzini, E. Bozzo, V. Burwitz, A. Castro-Tirado, E. Costa, T. Courvoisier, H. Feng, S. Gburek, R. Goosmann, V. Karas, G. Matt, F. Muleri, K. Nandra, M. Pearce, J. Poutanen, V. Reglero, D. Maria, A. Santangelo, G. Tagliaferri, C. Tenzer, J. Vink, .M.C. Weisskopf, S. Zane, I. Agudo, A. Antonelli, P. Attina, L. Baldini, A. Bykov, R. Carpentiero, E. Cavazzuti, E. Churazov, E. Del Monte, D. De Martino, I. Donnarumma, V. Doroshenko, Y. Evangelista, I. Ferreira, E. Gallo, N. Grosso, P. Kaaret, E. Kuulkers, J. Laranaga, L. Latronico, D.H. Lumb, J. Macian, J. Malzac, F. Marin, E. Massaro, M. Minuti, C. Mundell, J.U. Ness, T. Oosterbroek, S. Paltani, G. Pareschi, R. Perna, .P.-O. Petrucci, H.B. Pinazo, M. Pinchera, J.P. Rodriguez, M. Roncadelli, A. Santovincenzo, S. Sazonov, C. Sgro, D. Spiga, J. Svoboda, C. Theobald, T. Theodorou, R. Turolla, E. Wilhelmi de Ona, B. Winter, A.M. Akbar, H. Allan, R. Aloisio, D. Altamirano, L. Amati, E. Amato, E. Angelakis, J. Arezu, J.-L. Atteia, M. Axelsson, M. Bachetti, L. Ballo, S. Balman, R. Bandiera, X. Barcons, S. Basso, A. Baykal, W. Becker, E. Behar, B. Beheshtipour, R. Belmont, E. Berger, F. Bernardini, S. Bianchi, G. Bisnovatyi-Kogan, P. Blasi, P. Blay, A. Bodaghee, M. Boer, M. Boettcher, S. Bogdanov, I. Bombaci, R. Bonino, J. Braga, W. Brandt, A. Brez, N. Bucciantini, L. Burderi, I. Caiazzo, R. Campana, XIPE: the x-ray imaging polarimetry explorer, in: Proc. SPIE, Vol. 9905, in: Society of Photo-Optical Instrumentation Engineers (SPIE) Conference Series, Jul. 2016, p. 990515.
[7] E. Massaro, E. Del Monte, F. Massa, R. Campana, F. Muleri, P. Soffitta, E. Costa, Geometrical tools for the analysis of x-ray polarimetric signals, in: Space Telescopes and Instrumentation: Ultraviolet to Gamma Ray, in: Proc. SPIE, vol. 9905, Jul. 2016, p. 99054I.

[8] M. Weisskopf, R. Elsner, S. O'Dell, On understanding the figures of merit for detection and measurementof x-ray polarization, in: Proceedings of the SPIE, vol. 7732, pp. 77320E–77320E–5.
[9] R.F. Elsner, S.L. O'Dell, M.C. Weisskopf, Measuring x-ray polarization in the presence of systematic effects: known background, in: Space Telescopes and Instrumentation: Ultraviolet to Gamma Ray, in: Proc. SPIE, vol. 8443, Sep. 2012, p. 84434N.
[10] T.E. Strohmayer, T.R. Kallman, On the Statistical analysis of x-ray polarization measurements, Astrophys. J. 773 (2013) 103.
[11] F. Kislat, B. Clark, M. Beilicke, H. Krawczynski, Analyzing the data from X-ray polarimeters with Stokes parameters, Astropart. Phys. 68 (2015) 45–51.
[12] T.E. Strohmayer, X-ray spectro-polarimetry with photoelectric polarimeters, Astrophys. J. 838 (1) (2017) 72.
[13] J.E. Vaillancourt, Placing Confidence limits on polarization measurements, PASP 118 (2006) 1340–1343.
[14] D. Maier, C. Tenzer, A. Santangelo, Point and interval estimation on the degree and the angle of polarization: A bayesian approach, PASP 126 (2014) 459.
[15] F. Muleri, P. Soffitta, L. Baldini, R. Bellazzini, A. Brez, E. Costa, S. Fabiani, F. Krummenacher, L. Latronico, F. Lazzarotto, M. Minuti, M. Pinchera, A. Rubini, C. Sgró, G. Spandre, Spectral and polarimetric characterization of the Gas Pixel Detector filled with dimethyl ether, Nucl. Instrum. Methods Phys. Res. A 620 (2010) 285–293.
[16] S. Plaszczynski, L. Montier, F. Levrier, M. Tristram, A novel estimator of the polarization amplitude from normally distributed Stokes parameters, Mon. Not. R. Astron. Soc. 439 (2014) 4048–4056.
[17] E. Del Monte, A. Rubini, A. Brandonisio, F. Muleri, P. Soffitta, E. Costa, G. Di Persio, S. Di Cosimo, E. Massaro, A. Morbidini, E. Morelli, L. Pacciani, S. Fabiani, D. Michilli, S. Giarrusso, O. Catalano, D. Impiombato, T. Mineo, G. Sottile, S. Billotta, Silicon photomultipliers as readout elements for a Compton effect polarimeter: the COMPASS project, in: Society of Photo-Optical Instrumentation Engineers (SPIE) Conference Series. vol. 9915 of Proc. SPIE., 2016, p. 991528.